Jerash Geoarchaeology Working Paper 2: July 2018

Luminescence dating of soils and sediments from Jerash, Jordan

A.J. Cresswell[1], D.C.W. Sanderson[1], T.C. Kinnaird[1], G. Holdridge[2] A. Lichtenberger[3], R. Raja[4] and I. A. Simpson[1,5]

[1]*Scottish Universities Environment Research Centre, East Kilbride, Scotland, UK.*

[2]*Natural Sciences, Aarhus University, Denmark.*

[3]*Institut für Klassische Archäologie und Christliche Archäologie, Westfälische Wilhelms Universität Münster, Germany.*

[4]*School of Culture and Society – Centre for Urban Network Evolutions, Aarhus University, Denmark.*

[5]*Faculty of Natural Sciences and Centre for Environment, Heritage and Policy, University of Stirling, Stirling, Scotland, UK.*

1. Introduction

The urban site of Jerash, Jordan is recognised as one of the great cities of the classical Middle East and has been the subject of ongoing systematic archaeological investigations since the 1920s. Its significance lies in its location on limestone geology in one of the more fertile areas of the Ajlun Highlands in northern Jordan with a good water supply, a number of springs and its central position in regional trade routes. Earlier archaeological excavations focussed primarily on the monumental and public architecture of the Hellenistic, Roman, Byzantine and Islamic Ages to 749 AD, when the city was destroyed as a result of major seismic activity on the Jordan Valley strike - slip fault. Areas of domestic, everyday, activity in the early city had been largely ignored by the research community until the Northwest Quarter programme began excavation in the north-west part of the site during the summer of 2012. The environmental context of the site has not previously been considered, although the importance of the River Chrysorhous ("river of gold", presently known as Wadi Jerash or Wadi Suf) and a series of springs in the area to the rise and development of the ancient city have been acknowledged. Jerash is considered part of a comparative network of early urban sites (the UrbNet programme) from which new understandings of urban evolution are anticipated.

As part of these new and important research imperatives geoarchaeology has been introduced to the excavation programme at Jerash, and the wider UrbNet programme with the purpose of giving new insight into urban site formation processes and to explore relationships between the city and its hinterland within an urban evolution setting (Holdridge et al., 2017). To this purpose two field seasons (2015 and 2016) examined and sampled key stratigraphy in open archaeological investigations on the site and stratigraphy in Wadi Suf. Samples collected included those for Optically Stimulated Luminescence (OSL) measurement to give geo-chronological control on: 1) the formation processes associated with the Red Mediterranean Soils that underlie and are embedded within the urban Jerash site, and on 2) the sediment accumulation processes in Wadi Suf . Findings from these OSL analyses are reported here.

1

2. Study areas and stratigraphy

2.1. Soils and sediments underlying the city

Soil and sediment sections associated with the urban centre include Red Mediterranean Soil formed on the Na'ur limestone formation, over which colluvial and anthropogenic sediments are deposited. These soils and sediments offer a unique opportunity to consider landscapes prior to urban construction and have been sampled for thin section micromorphology and for bulk analyses. The regional Limestone geology (Abu-Jaber et al., 2009; Bender, 1974) does not include quartz or feldspar mineralogy essential to retain a luminescence signal and so our application of OSL as a dating tool is dependent aeolian-deposited quartz grains considered to have been have been deposited as Saharan dust during the Pleistocene and ceasing with the onset of the Holocene (Lucke et al., 2014; Issar et al., 1987; Issar and Bruins, 1983). Sampling for OSL measurement focussed on areas in the north-west quarter of the city (areas R, O, and Q), shown in Figure 1; a further sample was collected from the soils underlying the North Theatre (NT) cultural sediments; seven samples were collected for OSL measurement as summarised in Table 2.1, with field IDs and SUTL numbers assigned upon receipt at SUERC.
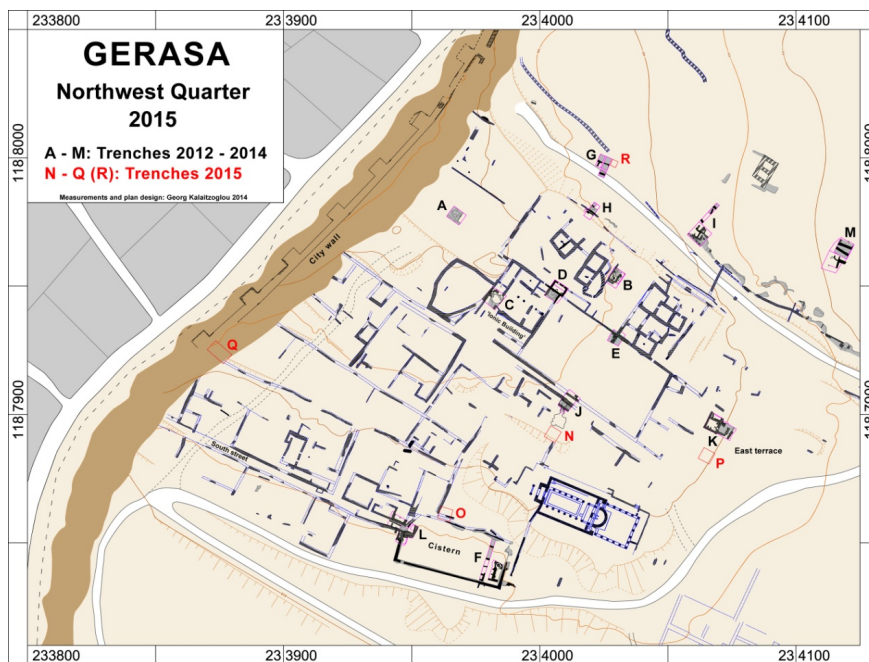
Area R is located in an open area of the north-west quarter within the city wall, and is thought to have functioned as an open space in the early city perhaps attached to a large unexcavated structure to the immediate east. Recognition of open areas are important as they may represent 'garden plots' known from elsewhere in Roman urban centres but so far missing from the Jerash archaeological record. The stratigraphy of interest is beneath an overburden created by bulldozing for the adjacent track or the 20th century fields.

Figure 1: Map of the Northwest quarter of Jerash, showing the location of the 2015 trenches.

The macro-stratigraphy is bedded at different angles and directions indicating attempts to modify slope characteristics. Based on field observation of sediment colour, texture, stoniness, sorting and cultural inclusion orientation we identified three contrasting red soil surfaces separated by fill material of fragmented limestone, cultural inclusions and grey soils; there is also indication of a thin underlying Red Mediterranean palaeosol at the base of the section and which rests on limestone bedrock. The uppermost red soil surface is an introduced Red Mediterranean A horizon [9]. This horizon shows fine material movement suggesting that this has been an open surface for an extended period of time. Linear orientation of pottery fragments indicated a second red soil surface in the stratigraphy (between [19] and [20]). This second red soil surface is short-lived but does indicate a

2

standstill phase in the infilling process. A third, lower, Red Mediterranean soil surface is characterised by a complex micro-sequence and with frequent charcoal inclusions [24 upper] and [24 lower]. These features, together with an absence of soil surface features, suggests that this material may have been deposited within an enclosed space and is part of domestic activity. At the base of the section, the thin Red Mediterranean soil would have covered the area prior to the city and which has largely been lost or substantially modified by urbanisation. A series of three OSL samples have been collected from contexts [9], [24] and [29] to frame the as yet unknown chronological sequence for this stratigraphy.

Area Q spans a section of the city wall, with excavations on either side of the wall offering a unique and important opportunity to examine soil stratigraphy immediately beneath and adjacent the wall. The excavations also revealed a water channel and pipe running from the wall into or out of the city, which were partially filled with sediment. Immediately outside the city wall and on the western face of the trench was an intact Red Mediterranean soil stratigraphy is evident beneath culturally deposited sediments. The upper phases (55 cm) are recent and likely associated with construction of the adjacent road; an earlier lower culturally deposited sediment is 30 cm in thickness. The Red Mediterranean soil has a 30 cm red A horizon separated by a sharp boundary from a 10 cm yellow B horizon beneath it. Below the B horizon is a yellow and stony B/C horizon, which is 15 cm thick and is situated over the limestone bedrock. This is considered to be a predominantly natural soil profile, although cultural modification associated with land management may be expected in A and B horizons. The section beneath the wall itself (east face) has a similar stratigraphy to the west face although with more variable A horizon thicknesses (10 - 30 cm and occasionally intermittent) above the yellow B horizon. There is also evidence of infill material to give a flatter surface for wall construction where Red Mediterranean soils are absent. The more variable attributes of this section are interpreted to relate to the wall building process. Inside and beneath the wall (east section) fill has been used to even out the terrain between limestone outcrops; an intermittent and thin (4 - 6 cm) Red Mediterranean soil is evident beneath the fill. This soil material can be traced across to the west section where an intact Red Mediterranean soil A horizon up to 40 cm thick and overlies associated B and B/C horizons beneath fill material.

Table 2.1: Samples IDs and summary descriptions for soil and sediment samples taken from strata underlying the urban structures at Jerash

Field ID	SUTL no. and (year)	Depth / cm	Summary Description
Area O Context [104]	2876 (2015)	1.5m	Red Mediterranean (Palaeo)-sol on limestone; associated with water channel and large cistern.
Area R Context [29]	2877 (2015)	2.40m	Overburden of 2.40m; 0.1m above limestone bedrock; Limestone clasts throughout stratigraphy
Area R Context [24]	2878 (2015)	1.80m	Overburden of 1.80m; 0.9m above limestone bedrock; Limestone clasts throughput stratigraphy
Area R Context [9]	2879 (2015)	0.80m	Overburden of 0.80m; 1.75m above limestone bedrock; Limestone clasts throughout stratigraphy
Area Q [Inner]	2880 (2015)	Wall is 5.2 m in height	Red Mediterranean (Palaeo)-sol; located immediately beneath city wall and on limestone, inside area of wall. Wall is constructed of limestone
Area Q [Outer]	2881 (2015)	Wall is 5.2 m in height	Red Mediterranean (Palaeo)-sol; located immediately beneath city wall and on limestone, outside area of wall. Wall is constructed of limestone
JD16 (2) NT1 [18]	2962 (2016)	Urban environment, colluvial sediments below city and adjacent North Theatre	Dating of colluvial sediments, beneath urban sediments, allowing assessment of whether a sediments based environmental record can be constructed.

Area O is associated with located what is thought to be a large open cistern area and is characterised by a series of clearly evident constructed water channels (both open and closed) and by a sediment trap leading to the cistern over which are superimposed structures. Relationships between these different water flow structures are still unclear. Samples of Red Mediterranean soil beneath the structure were obtained for OSL, thin section micromorphology, and bulk analyses in order to examine the soils underlying the urban site and to give context to the introduction of the constructed water channels which these soils may predate.

Area NT comprise cultural sediments that accumulated behind the Roman North Theatre of Jerash city. Underlying these sediments was a Red Mediterranean Soil with an 'A' horizon directly superimposed on limestone bedrock. Immediately on top of the buried 'A' horizon was a colluvial deposit with cultural inclusions. Samples for OSL dating were taken from the lower part of the colluvial deposit with a view to dating sediment accumulation prior to the onset of cultural deposition. It was also anticipated that this deposit may give a chronological link from the urban site to the sediment accumulations in the wadi.

2.2. Wadi Suf / Wadi Jerash soils and sediments

A survey of soil / sediment profiles in the wadi has been undertaken. Three to four kilometers north of Jerash, recent modifications of the wadi channel revealed fluvial sediments with a range of particle sizes from cobbles to silty loams indicating variances in deposition energy environments. There are also substantial thicknesses of colluvial deposits incorporating Red Mediterranean soils material.
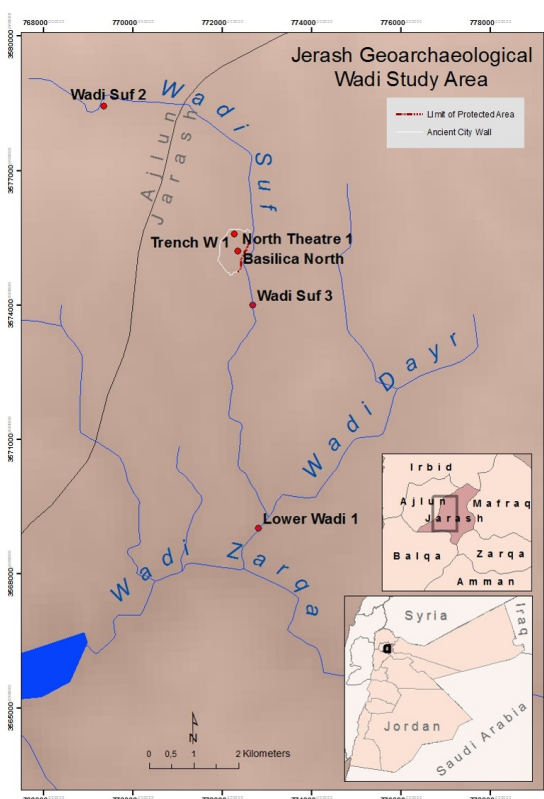

Figure 2: Wadi Suf / Wadi Jerash sample Locations

The limestone geology associated with upper section of Wadi Suf contains no quartz or feldspar mineralogy. Therefore, similar to the on-site samples, OSL measurement relies on aeolian-deposited Pleistocene deposited quartz grains for the retention of luminescence signals. The lower Wadi also has lower local quartzose sandstone outcrops (Kumub) contributing to the quartz-based OSL signal (Abu-Jaber et al., 2009; Amireh, 1997; Bender, 1974). Samples for OSL measurement were collected at three locations within the Wadi Suf catchment from exposed sections upstream and immediately down stream of the ancient city, as well as further downstream just beyond the junction of Wadi Suf and Wadi Dayr. The locations of the sampled sections allows for downstream variations in the material characteristics of the target dosimeters (for luminescence dating) to be investigated, which may reveal new information on sediment transport processes and deposition within the wadi. These investigations provide the temporal framework to interpret wadi sediment formation processes based on subsequent luminiescence profiling and, importantly, the means to assess the sensitivity of the wadi system to natural and human change. Seven samples were collected from the wadi stratigraphy for OSL data as summarised in Table 2.2.

4

Table 2.2: Samples IDs and descriptions for the Wadi Suf / Wadi Jerash OSL analyses

Field ID	SUTL no. and (year)	SummaryDescription
JD16 (1) WS2 [5]	2961 (2016)	Wadi environment, colluvial and alluvial sediments exposed by stream and water management works. Sample from upper alluvial
WS2Lower 3.10m	2882 (2015)	Alluvial sands, from Wadi sequence of colluvial and alluvial sediments; exposed by stream and water management works; sample taken from lower alluvial sands superimposed on limestone bedrock.
JD16 (3) WS3 [4]	2963 (2016)	Wadi environment, colluvial and alluvial sediments exposed by stream incision (fix below). Sample from upper alluvial
JD16 (4) WS3 [9]	2964 (2016)	Wadi environment, colluvial and alluvial sediments cut by stream. Sample from lower alluvial
JD16 (5) LW1 [4]	2965 (2016)	Wadi environment, colluvial and alluvial sediments cut by stream. Sample from upper alluvial
JD16 (6) LW1 [23]	2966 (2016)	Wadi environment, colluvial and alluvial sediments cut by stream. Sample from lower alluvial
JD16 (7) LW1 [25]	2967 (2016)	Wadi environment, colluvial and alluvial sediments cut by stream. Sample from lower alluvial

3. Optically Stimulated Luminescence measurement

3.1 Dose Rate Determination

Dose rate determination was undertaken using thick source beta counting (TSBC) and high resolution gamma spectrometry (HRGS). For the samples collected in 2015 and 2016?, dose rate measurements were conducted on tube samples, while measurements were also conducted on associated bulk material on the samples collected in 2016 .

Beta dose rates were measured directly using the SUERC TSBC system (Sanderson, 1988). Sample count rates were determined with six replicate 600 s counts for 20 g of each sample, bracketed by background measurements and sensitivity determinations using the Shap Granite secondary reference material. Infinite-matrix dose rates were calculated by scaling the net count rates of samples and reference material to the working beta dose rate of the Shap Granite (6.25 ± 0.03 mGy a^{-1}). The estimated errors combine counting statistics, observed variance and the uncertainty on the reference value.

Following TSBC, the 20 g samples were included in ~50 g of material sealed in polypropylene containers using epoxy resin and left for three weeks to allow radon daughter equilibration. HRGS measurements were performed using a 50% relative efficiency "n" type hyper-pure Ge detector (EG&G Ortec Gamma-X) operated in a low background lead shield with a copper liner. Gamma ray spectra were recorded over the 30 keV to 3 MeV range from each sample, interleaved with background measurements and measurements from SUERC Shap Granite standard in the same geometries. Sample counts were made in duplicate over 80 ks. The spectra were analysed to determine count rates from the major line emissions from ^{40}K (1461 keV), and from selected nuclides in the U decay series (^{234}Th, ^{226}Ra + ^{235}U, ^{214}Pb, ^{214}Bi and ^{210}Pb) and the Th decay series (^{228}Ac, ^{212}Pb, ^{208}Tl) and their statistical counting uncertainties. Net rates and activity concentrations for each of these nuclides were determined relative to Shap Granite by weighted combination of the individual lines for each nuclide. The internal consistency of nuclide specific estimates for U and Th

decay series nuclides was assessed relative to measurement precision, and weighted combinations used to estimate mean activity concentrations (Bq kg^{-1}) and elemental concentrations (% K and ppm U, Th) for the parent activity. These data were used to determine infinite matrix dose rates for alpha, beta and gamma radiation.

The dose rate measurements were used, in combination with the grain size and assumed burial water contents, to determine the overall effective dose rates for age estimation. Cosmic dose rates were modelled by combining latitude and altitude specific dose rates for the site with corrections for estimated depth of overburden using the method of Prescott and Hutton (1994).

3.2 Quartz SAR luminescence measurements

Minerals were extracted and quartz grains purified for dose determination using a single aliquot regenerative (SAR) procedure.

3.2.1   Sample Preparation

Approximately 10 g of material was removed for each sample and processed to obtain sand-sized quartz grains for luminescence measurements. Each sample was wet sieved to obtain the 90-150 and 150-250 μm fractions. The 150-250 μm fractions were treated with 1 M hydrochloric acid (HCl) for 10 minutes, 15% hydrofluoric acid (HF) for 15 minutes, and 1 M HCl for a further 10 minutes. The HF-etched sub-samples were then centrifuged in sodium polytungstate solutions of ~2.64, and 2.74 g cm^{-3}, to obtain concentrates of feldspars (<2.64 g cm^{-3}), and quartz plus plagioclase (2.64-2.74 g cm^{-3}). The selected quartz fraction was then subjected to further HF and HCl washes (40% HF for 40 mins, followed by 1M HCl for 10 mins).

All materials were dried at 50°C and transferred to Eppendorf tubes. The 40% HF-etched, 2.64-2.74 g cm^{-3} 'quartz' 150-250 μm fractions were dispensed to 10 mm stainless steel discs for measurement. 16 aliquots were dispensed for each sample. The purity of which was checked using a Hitachi S-3400N scanning electron microscope (SEM), coupled with an Oxfords Instruments INCA EDX system, to determine approximate elemental concentrations for each sample.

3.2.2   SAR measurements

All measurements were conducted using a Risø DA-15 automatic reader equipped with a ^{90}Sr/^{90}Y β-source for irradiation, blue LEDs emitting around 470 nm and infrared (laser) diodes emitting around 830 nm for optical stimulation, and a U340 detection filter pack to detect in the region 270-380 nm, while cutting out stimulating light (Bøtter-Jensen et al., 2000).

Equivalent dose determinations were made on sets of 16 aliquots per sample, using a single aliquot regeneration (SAR) sequence (cf Murray and Wintle, 2000). Using this procedure, the OSL signal levels from each individual disc were calibrated to provide an absorbed dose estimate (the equivalent dose) using an interpolated dose-response curve, constructed by regenerating OSL signals by beta irradiation in the laboratory. Sensitivity changes which may occur as a result of readout, irradiation and preheating (to remove unstable radiation-induced signals) were monitored using small test doses after each regenerative dose. Each measurement was standardised to the test dose response determined immediately after its readout, to compensate for changes in sensitivity during the laboratory measurement sequence. The regenerative doses were chosen to encompass the likely value

6

of the equivalent (natural) dose. A repeat dose point was included to check the ability of the SAR procedure to correct for laboratory-induced sensitivity changes (the 'recycling test'), a zero dose point is included late in the sequence to check for thermally induced charge transfer during the irradiation and preheating cycle (the 'zero cycle'), and an IR response check included to assess the magnitude of non-quartz signals. Regenerative dose response curves were constructed using doses of 1.0, 2.5, 5.0, 10, and 20 Gy, with test doses of 1.0 Gy. The 16 aliquot sets were sub-divided into four subsets of four aliquots, such that four preheating regimes were explored (220°C, 240°C, 260°C and 280°C).

4   Results

4.1 Dose Rate Measurements

The activity concentrations determined by HRGS are given in Table 4.1. It can be seen that the K concentration for the wadi sediments (SUTL2882, SUTL2961-2967) are generally lower than for the occupation related contexts, 40-180 Bq kg^{-1} cf 250-380 Bq kg^{-1} excluding SUTL2877.

Table 4.1: Activity and equivalent concentrations of K, U and Th determined by HRGS (for SUTL2961-2967 showing the tube, top, and bulk samples)

SUTL no.	Activity Concentration[a] / Bq kg^{-1}			Equivalent Concentration[b]		
	K	U	Th	K / %	U / ppm	Th / ppm
2876	452 ± 16	38.4 ± 2.4	29.2 ± 1.4	1.46 ± 0.05	3.11 ± 0.19	7.20 ± 0.34
2877	118 ± 12	12.5 ± 1.1	7.5 ± 1.2	0.38 ± 0.04	1.01 ± 0.09	1.84 ± 0.30
2878	277 ± 24	15.5 ± 1.6	12.3 ± 1.4	0.90 ± 0.08	1.25 ± 0.13	3.03 ± 0.36
2879	287 ± 15	23.1 ± 1.6	19.0 ± 1.4	0.93 ± 0.05	1.87 ± 0.13	4.69 ± 0.34
2880	376 ± 15	27.2 ± 1.8	22.6 ± 1.5	1.22 ± 0.05	2.20 ± 0.14	5.57 ± 0.36
2881	253 ± 14	19.7 ± 1.5	16.5 ± 1.4	0.82 ± 0.05	1.60 ± 0.12	4.06 ± 0.34
2882	100 ± 12	19.2 ± 1.5	7.6 ± 1.2	0.32 ± 0.04	1.56 ± 0.12	1.87 ± 0.29
2961	128 ± 13	18.3 ± 1.4	15.1 ± 1.3	0.41 ± 0.04	1.48 ± 0.11	3.73 ± 0.32
	141 ± 8	20.0 ± 1.0	11.3 ± 0.7	0.45 ± 0.03	1.62 ± 0.08	2.78 ± 0.17
2962	176 ± 12	12.1 ± 1.2	7.5 ± 1.3	0.57 ± 0.04	0.98 ± 0.10	1.84 ± 0.32
	181 ± 8	12.0 ± 0.8	6.4 ± 0.6	0.58 ± 0.03	0.97 ± 0.07	1.58 ± 0.16
2963	147 ± 12	16.6 ± 1.3	14.4 ± 1.4	0.48 ± 0.04	1.35 ± 0.10	3.55 ± 0.33
	93 ± 7	12.9 ± 0.9	8.8 ± 0.6	0.30 ± 0.02	1.04 ± 0.07	2.17 ± 0.16
2964	123 ± 11	16.1 ± 1.3	14.4 ± 1.3	0.40 ± 0.04	1.31 ± 0.10	3.55 ± 0.32
	116 ± 10	22.2 ± 1.3	10.8 ± 0.9	0.37 ± 0.03	1.8 ± 0.11	2.67 ± 0.22
2965	93 ± 10	26.0 ± 1.4	16.8 ± 1.4	0.30 ± 0.03	2.11 ± 0.12	4.13 ± 0.33
	88 ± 10	27.9 ± 1.4	13.6 ± 1.1	0.28 ± 0.03	2.26 ± 0.11	3.36 ± 0.27
2966	33 ± 10	13.3 ± 1.2	11.5 ± 1.3	0.11 ± 0.03	1.08 ± 0.10	2.84 ± 0.32
	49 ± 6	20.8 ± 1.0	7.6 ± 0.7	0.16 ± 0.02	1.68 ± 0.08	1.87 ± 0.16
2967	42 ± 10	17.7 ± 1.3	11.0 ± 1.3	0.14 ± 0.03	1.44 ± 0.10	2.71 ± 0.31
	41 ± 7	21.6 ± 1.3	11.7 ± 1.0	0.13 ± 0.02	1.75 ± 0.11	2.89 ± 0.24

[a]Shap granite reference, working values determined by David Sanderson in 1986, based on HRGS relative to CANMET and NBL standards.
[b]Activity and equivalent concentrations for U, Th and K determined by HRGS (Conversion factors based on NEA (2000) decay constants): 40K: 309.3 Bq kg^{-1} %K^{-1}, 238U: 12.35 Bq kg^{-1} ppmU^{-1}, 232Th: 4.057 Bq kg^{-1} ppm Th^{-1}

The dry infinite matrix dose rates calculated from these concentrations are given in Table 4.2, along with the dry beta dose rate from TSBC. The beta dose rates from HRGS and TSBC are in reasonable agreement for the 2015 samples (SUTL2876-2882), whereas for the 2016 samples (SUTL2961-2967) the TSBC value is generally larger than the HRGS by typically 40%. The HRGS data do not indicate disequilibrium in the uranium or thorium series, which could result in a

difference between HRGS and TSBC. It is noted that the samples include significant amounts of limestone, with relatively large clasts that were roughly ground prior to TSBC measurement. Non-uniform distribution of beta emitting nuclides within the sample can also result in differences between TSBC and HRGS. It is known that limestone clasts can result in more complicated beta micro-dosimetry. Beta and gamma dose rates for the Wadi Suf samples are generally lower than for the 2015 samples from locations associated with occupation. It is noted that SUTL2877, the palaeosol at the base of area R is more similar to the Wadi Suf sediments than the other occupation related samples.

4 4.2: Infinite matrix dose rates determined by HRGS and TSBC

SUTL no.	HRGS, dry[a] / mGy a^{-1}			TSBC, dry / mGy a^{-1}	FGS, wet / mGy a^{-1}
	Alpha	Beta	Gamma		
2876	13.96 ± 0.60	1.87 ± 0.05	1.08 ± 0.03	1.76 ± 0.08	0.36 ± 0.03
2877	4.17 ± 0.33	0.52 ± 0.04	0.30 ± 0.02	0.35 ± 0.06	0.24 ± 0.02
2878	5.73 ± 0.44	1.01 ± 0.07	0.52 ± 0.03	1.25 ± 0.06	0.32 ± 0.03
2879	8.67 ± 0.45	1.18 ± 0.04	0.68 ± 0.03	1.29 ± 0.08	0.32 ± 0.03
2880	10.23 ± 0.48	1.49 ± 0.05	0.83 ± 0.03	1.22 ± 0.08	0.36 ± 0.03
2881	7.44 ± 0.42	1.03 ± 0.04	0.59 ± 0.02	1.03 ± 0.08	0.26 ± 0.02
2882	5.71 ± 0.39	0.55 ± 0.04	0.35 ± 0.02	0.39 ± 0.07	0.27 ± 0.02
2961	6.72 ± 0.23	0.68 ± 0.02	0.45 ± 0.01	0.97 ± 0.05	0.27 ± 0.02
2962	3.98 ± 0.21	0.67 ± 0.02	0.34 ± 0.01	1.08 ± 0.05	0.27 ± 0.02
2963	5.43 ± 0.22	0.58 ± 0.02	0.38 ± 0.01	1.01 ± 0.05	0.27 ± 0.02
2964	6.62 ± 0.25	0.64 ± 0.02	0.43 ± 0.01	0.89 ± 0.05	0.27 ± 0.02
2965	8.84 ± 0.28	0.67 ± 0.02	0.51 ± 0.02	0.78 ± 0.05	0.36 ± 0.03
2966	5.58 ± 0.22	0.38 ± 0.02	0.31 ± 0.01	0.55 ± 0.05	0.26 ± 0.02
2967	6.50 ± 0.25	0.42 ± 0.02	0.36 ± 0.01	0.44 ± 0.04	0.24 ± 0.02

[a]based on dose rate conversion factors in Aitken (1983) and Sanderson (1987)

The measured and assumed water contents are given in Table 4.3. For the samples from the Wadi Suf, (SUTL2882, SUTL2961-2967) the field water contents are similar (0-3%) with the majority of saturated water contents in the 20-25% range. Water content for all the 2016 samples was assumed to be the same since there was so little difference in the measured values.

Table 4.3: Water contents

SUTL no.	Water contents / %		
	Field	Saturated	Assumed
2876	10.4	24.5	17 ± 6
2877	3.2	15.8	10 ± 6
2878	9.2	23.9	17 ± 7
2879	8.0	30.1	20 ± 7
2880	10.6	20.0	15 ± 5
2881	11.8	23.3	18 ± 6
2882	3.0	23.2	13 ± 6
2961	2.3	22.7	15 ± 10
2962	1.7	12.4	15 ± 10
2963	1.2	44.7	15 ± 10
2964	2.9	9.3	15 ± 10
2965	1.0	23.8	15 ± 10
2966	0.1	22.8	15 ± 10
2967	2.4	28.8	15 ± 10

The effective dose rates accounting for water content and grain size are given in Table 4.4, for 150-250 μm grains. Where samples are recorded as being collected in close vicinity of the limestone bedrock additional weighting has been applied to the field gamma spectrometry data. The total dose

rates include a cosmic dose rate contribution. For the 2016 samples (SUTL2961-2967) in the absence of sample location information the mean cosmic dose rate for the 2015 samples (0.11 ± 0.02 mGy a^{-1}) has been used.

Table 4.4: Effective beta and gamma dose rates following water correction

SUTL no.	Effective Dose Rate[a] / mGy a^{-1}		
	Beta	Gamma	Total[c]
2876	1.41 ± 0.09	0.63 ± 0.06	2.16 ± 0.11
2877	0.36 ± 0.04	0.25 ± 0.02[b]	0.71 ± 0.04
2878	0.87 ± 0.10	0.38 ± 0.05	1.36 ± 0.11
2879	0.92 ± 0.07	0.44 ± 0.05	1.49 ± 0.09
2880	1.06 ± 0.07	0.45 ± 0.03	1.59 ± 0.07
2881	0.78 ± 0.06	0.32 ± 0.03[b]	1.18 ± 0.07
2882	0.37 ± 0.04	0.29 ± 0.03[b]	0.76 ± 0.05
2961	0.64 ± 0.08	0.33 ± 0.05	1.06 ± 0.09
2962	0.69 ± 0.08	0.28 ± 0.04	1.06 ± 0.09
2963	0.62 ± 0.08	0.30 ± 0.04	1.00 ± 0.09
2964	0.59 ± 0.08	0.32 ± 0.04	1.00 ± 0.09
2965	0.55 ± 0.07	0.40 ± 0.05	1.04 ± 0.09
2966	0.35 ± 0.06	0.26 ± 0.04	0.71 ± 0.07
2967	0.33 ± 0.05	0.28 ± 0.04	0.70 ± 0.07

[a] Effective beta dose rate combining water content corrections with inverse grain size attenuation factors obtained by weighting the 200 μm attenuation factors of Mejdahl (1979) for K, U, and Th by the relative beta dose contributions for each source determined by Gamma Spectrometry;
[b] weighted 3:1 between FGS: HRGS, due to proximity to carbonate bedrock lithologies
[c] includes a cosmic dose contribution (0.11 ± 0.03 - mean of 2015 depth corrected dose rates applied to all in absence of sample descriptions including burial depth)

4.2   SAR Dose Estimation

Quality parameters for the SAR analyses are given in Table 4.5. These samples are generally bright, with sensitivities for the occupation related samples of ~15 kc Gy^{-1}, with lower sensitivities for the Wadi Suf sediments. Sensitivity changes through the measurement cycles are generally small, recycling ratios consistent with unity, no signal from the zero dose cycle, in most cases no significant IRSL signal and good dose recovery behaviour. The dose response curves (Appendix A) show saturating exponential fits through points with little pre-heat temperature variation.

Individual equivalent dose estimates were determined for aliquots that satisfied the SAR quality criteria and had natural signals which were not in saturation. The mean equivalent dose for each sample was determined using linear, weighted and robust statistics (Table 4.6). The distributions of equivalent dose determinations are illustrated using Kernal Density Estimate (KDE) and Probability Density Function (PDF) plots (Appendix B) and Abanico plots (Appendix C). Table 4.6 summarises the dose distributions illustrated in Appendices B and C, with the best estimate for the equivalent dose indicated in bold.

It is evident that there is a substantial scatter in individual dose estimates for most samples, with many aliquots saturated. This suggests that the samples represent mixed-age sediments, carrying residual signals. To attempt to resolve the different dose components some small aliquot SAR measurements were also conducted.

Scottish Universities Environmental Research Centre

Table 4.5: SAR quality parameters, where two sets of parameters are given the lower set are for small aliquot data.

SUTL no.	Sensitivity / counts Gy[1]	Sensitivity change /%	Recycling ratio	Zero dose	Dose recovery	IRSL response / %
2876	16369 ±9209	12.7 ± 2.1	1.00 ± 0.03	0.01 ± 0.00	1.03 ± 0.05	1.3 ± 4.6
2877	13430 ±8972	23.8 ± 8.8	0.96 ± 0.05	0.04 ± 0.02		0.8 ± 2.7
2878	14670 ±7841	5.2 ± 0.9	1.01 ± 0.05	0.01 ± 0.01		14.9±55.9
2879	14285 ±9546	12.6 ± 4.6	1.00 ± 0.05	0.01 ± 0.01		0.2 ± 0.4
2880	13416±11995	10.9 ± 8.1	1.01 ± 0.04	-0.01 ±0.08		0.1 ± 0.4
2881	14101±15047	1.6 ± 0.4	1.00 ± 0.05	0.01 ± 0.01		0.1 ± 0.4
2882	2066±2213	12.3±10.3	1.00 ± 0.06	0.02 ± 0.06		0.3 ± 1.4
2961	5529 ± 514	9.6 ± 3.7	1.01 ± 0.02	0.02 ± 0.01	0.98 ± 0.03	-0.5 ± 0.1
2962	5238 ± 523	6.3 ± 3.6	1.02 ± 0.02	0.02 ± 0.01	1.02 ± 0.02	0.4 ± 0.1
2963	10989 ± 1645	4.2 ± 5.0	1.02 ± 0.01	0.02 ± 0.01	1.03 ± 0.02	0.2 ± 0.1
2964	1675 ± 204	-1.3 ± 3.3	0.96 ± 0.03	0.05 ± 0.02	1.37 ± 0.10	3.1 ± 0.8
	817 ± 83	-2.3 ± 0	1.01 ± 0.05	0.03 ± 0.06	1.23 ± 0.13	-0.5 ± 3.7
2965	2511 ± 432	2.3 ± 5.4	0.95 ± 0.02	0.07 ± 0.07	1.17 ± 0.12	-1.2 ± 1.6
	1411 ± 259	5.6 ± 0.1	1.01 ± 0.06	0.00 ± 0.04	1.16 ± 0.07	0.5 ± 1.8
2966	692 ± 40	-5.2 ± 1.4	0.99 ± 0.04	0.04 ± 0.08	1.45 ± 0.14	3.3 ± 2.0
2967	2708 ± 772	5.3 ± 9.9	0.98 ± 0.03	0.08 ± 0.02	1.05 ± 0.08	1.0 ± 0.7

Table 4.6: Summary of dose distributions and mean equivalent doses, with the preferred value indicated by bold type

SUTL no.	Description of dose distribution	Mean Equivalent dose (Gy)		
		Linear	Weighted	Robust
2876	Narrow peak at ~5 Gy	5.12 ± 0.21	**4.98 ± 0.07**	5.12 ± 0.21
2877	Narrow peak at ~2 Gy with tail to higher doses	3.23 ± 0.50	**2.16 ± 0.06**	2.14 ± 0.24
2878	Narrow peak at ~3 Gy with tail to higher doses	3.48 ± 0.18	**3.10 ± 0.05**	3.10 ± 0.21
2879	Very broad distribution ~5-40 Gy	16.33 ± 7.24	**9.74 ± 2.96**	16.33 ± 6.92
2880	Cluster of aliquots at ~3-4 Gy, with second cluster at ~5-9 Gy	4.48 ± 1.31	**3.97 ± 0.41**	4.48 ± 1.51
2881	Very broad distribution 0-40 Gy, no defined peak or grouping	21.7 ± 13.2	**9.85 ± 3.02**	20.2 ± 11.2
2882	Narrow peak at ~1 Gy with tail to higher doses	1.25 ± 0.71	**1.05 ± 0.16**	1.09 ± 0.41
2961	Multiple peaks in distribution between 1-5 Gy. One aliquot >45 Gy. A cluster of five aliquots form a low dose peak at 1.0-1.5 Gy, the mean of these is **1.30 ± 0.02** Gy	4.87 ± 2.76	1.70 ± 0.04	2.15 ± 0.01
2962	Multiple peaks in distribution between 0-8 Gy, with a small number of low precision measurements at higher doses. A cluster of four aliquots form a low dose peak at ~2.5 Gy, with a single lower dose aliquot, the mean of these is **2.40 ± 0.02** Gy.	4.64 ± 0.75	2.01 ± 0.04	4.12 ± 0.13
2963	PDF shows multiple peaks 0-3 Gy. KDE and abanico plots show most aliquots fall within a single peak 0-1.5 Gy.	1.35 ± 0.35	**0.62 ± 0.01**	0.99 ± 0.01
2964	Large aliquots. Very broad distribution. 7 aliquots saturated.	25.62 ± 2.95	16.45 ± 2.23	25.62 ± 0.57
	Small aliquots. PDF shows dominant peak ~5-6 Gy with long tail to higher dose with secondary peaks and 11 saturated aliquots. KDE and abinico plots show distribution around weighted mean with higher dose components.	24.74 ± 5.52	**4.76 ± 1.63**	24.74 ± 1.65
2965	Large (16) aliquots. PDF single low dose point (0.26 Gy), with a peak at ~1 Gy from four points. Long tail and one saturated aliquot.	2.60 ± 0.55	0.35 ± 0.05	2.46 ± 0.18
	Small aliquots. PDF shows dominant peak ~1 Gy, with long tail to higher dose with secondary peaks and one saturated aliquot. KDE and abinico plots show distribution around weighted mean with higher dose components.	3.57 ± 0.83	**1.33 ± 0.11**	3.56 ± 0.04
2966	Broad distribution, three saturated aliquots.	32.52 ± 2.50	**25.26 ± 3.35**	31.87 ± 0.62
2967	Single high precision low dose point (0.62 Gy), with peaks at 1-2 Gy (6 aliquots, mean **1.77 ± 0.12** Gy) and ~8 Gy, and long tail	4.10 ± 0.76	0.69 ± 0.03	4.10 ± 0.23

5 Discussion and conclusions

The ages of the sediments determined by the best estimate equivalent dose (Table 4.6) to the dose rate (Table 4.4) are given in Table 5.1 and represent the period when the sediment was last exposed to light.

Table 5.1: Soil and sediment ages, Jerash data set

Field ID	SUTL no.	Dose rate /mGy a⁻¹	Equivalent dose /Gy	Age /ka	Age /calendar years
Soils and sediments underlying the city					
Area O Context [104]	2876	2.16 ± 0.11	4.98 ± 0.07	2.31 ± 0.13	300 ± 130 BC
Area R Context [29]	2877	0.71 ± 0.04	2.16 ± 0.06	3.02 ± 0.20	1010 ± 200 BC
Area R Context [24]	2878	1.36 ± 0.11	3.10 ± 0.05	2.27 ± 0.18	260 ± 180 BC
Area R Context [9]	2879	1.49 ± 0.09	9.74 ± 2.96	6.56 ± 2.03	4540 ± 2030 BC
Area Q [Inner]	2880	1.59 ± 0.07	3.97 ± 0.41	2.50 ± 0.28	480 ± 280 BC
Area Q [Outer]	2881	1.18 ± 0.07	9.85 ± 3.02	8.35 ± 2.60	6330 ± 2600 BC
JD16 (2) NT1 [18]	2962	1.06 ± 0.09	2.40 ± 0.02	2.26 ± 0.19	250 ± 190 BC
Wadi Suf / Wadi Jerash soils and sediments					
WS2Profile 2 Lower	2882	0.76 ± 0.05	1.05 ± 0.16	1.38 ± 0.24	640 ± 240 AD
JD16 (1) WS2 [5]	2961	1.06 ± 0.09	1.30 ± 0.02	1.23 ± 0.11	790 ± 110 AD
JD16 (3) WS3 [4]	2963	1.00 ± 0.09	0.62 ± 0.01	0.62 ± 0.06	1400 ± 60 AD
JD16 (4) WS3 [9]	2964	1.00 ± 0.09	4.76 ± 1.63	4.76 ± 1.69	2740 ± 1690 BC
JD16 (5) LW1 [4]	2965	1.04 ± 0.09	1.33 ± 0.11	1.28 ± 0.15	740 ± 150 AD
JD16 (6) LW1 [23]	2966	0.71 ± 0.07	25.3 ± 3.4	35.6 ± 5.9	33600 ± 5900 BC
JD16 (7) LW1 [25]	2967	0.70 ± 0.07	1.77 ± 0.12	2.53 ± 0.31	510 ± 310 BC

5.1 Soils and sediments underlying the city

Two samples from this set (SUTL2879 and SUTL2881; Table 5.1) show anomalously old ages with very large uncertainties and we suggest that these measurements show natural background variances in exposure of the sediment to light over extended periods of time. The remaining five samples have much less variance and are much more likely to have exposures to light that are associated with more precisely defined periods.

On this basis we suggest an early disturbance and covering of the landscape dated to 3.02 ± 0.20 ka (SUTL2877; 1010 ± 200 BC; Table 5.1) with the subsequent transport of this material to Area R failing to expose the sample to light. Four measurements (SUTL2876; SUTL2878; SUTL2880; SUTL2962; Table 5.1) are clustered within a range of ca. 480 BC – 250 BC with three of these clustered between ca. 250 BC and 300 BC. These observations suggest a sustained and spatially persistent covering of the landscape coinciding with the founding and development of the Hellenistic city.

5.2 Wadi Suf / Wadi Jerash soils and sediments

As with the soils and sediments underlying the city, two samples from Wadi Suf / Wadi Jerash also show anomalously old ages with very large uncertainties (SUTL2964 and SUTL2966; Table 5.1); again we suggest that these measurements show natural background variances in exposure of the sediment to light over extended periods of time. The very early date of 33600 ± 5900 BC is of

particular geomorphological interest indicating aeolian accumulations of quartz were occurring during the later Pleistocene.

Our measurements suggest a variable period of sediment accumulation into the lower wadi at 510 ± 310 BC (SUTL2967) but the dominant trend in upper, mid and lower wadi locations is the sediment infilling of the wadi between 640 ± 240 AD and 1400 ± 60 AD. This is particularly noticeable in the upper wadi samples, above Jerash, where sediment ages of 1.38 to 1.23 ka (640 - 790 AD; SUTL2961, SUTL2882) lie directly above bedrock. Accumulation of sediments in the mid wadi locations was occurring at 1400 ± 60 AD (SUTL2963 and in the lower wadi from 740 ± 150 AD (SUTL2965). These observations suggest that major movement of sediments rapidly filled the upper wadi with accelerated accumulations in the mid and lower wadi locations after the ending of the Byzantine period. Our explanation of this significant phase of sediment movement and accumulation is the decline and loss of land management controls in the agricultural hinterland of Jerash, paralleling the decline of city after the earthquake of 749 AD. This also serves to highlight the effectiveness of Roman and Byzantine land management in what was and is a soil environment sensitive to degradation.

References

Abu-Jaber, N., al-Saad, Z. and Smadi, N., 2009, The quarryscapes of Gerasa (Jarash), Jordan. In: Abu-Jaber, N., Bloxam, E. G., Degryse, P. and Heldal, T. (eds.) QuarryScapes: ancient stone quarry landscapes in the Eastern Mediterranean, Geological Survey of Norway Special publication,12, pp. 67–75

Aitken, M.J., 1983, Dose rate data in SI units: PACT, v. 9, p. 69–76.

Amireh, B.S., 1997, Sedimentology and palaeogeography of the regressive-transgressive Kurnub Group (Early Cretaceous) of Jordan. Sedimentary Geology 112 69-88

Bender, F., 1974, Geology of Jordan. Gebrüder Bornträger, Berlin

Holdridge, G., Kristiansen, S.M., Lichtenberger, A., Raja, R. and Simpson, I.A., 2017, City and wadi, exploring the environs of Jerash. *Antiquity* 91, 1-6. doi:10.15184/aqy.2017.123

Issar, A.S., Bruins, H.J., 1983, Special climatological conditions in the deserts of Sinai and the Negev during the Latest Pleistocene. Paleogeography, Palaeoclimatology, Palaeoecology 43, 63–72.

Issar, A., Tsoar, C., Gilead, I., Zangvil, A., 1987, A paleoclimatic model to explain depositional environments during Late Pleistocene in the Negev. In: Berkofsky, L., Wurtele, G. (Eds.), Progress in Desert Research. Rowman& Littlefield, Totowa, pp. 302–309.

Lucke, B., Kemnitz, H., Bäumler, R., and Schmidt, M., 2014, Red Mediterranean soils in Jordan: new insights in their origin, genesis, and role as environmental archives. Catena 112: 4–24.

Mejdahl, V., 1979, Thermoluminescence daing: Beta-dose attenuation in quartz grains Archaeometry, v. 21, p. 61-72.

Mejdahl, V., 1983, Feldspar inclusion dating of ceramics and burnt stones, PACT, v. 9, p. 351-364. NEA, 2000, The JEF-2.2 Nuclear Data Library: Nuclear Energy Agency, Organisation for economic Co-operation and Development. JEFF Report, v. 17.

Prescott, J.R., and Hutton, J.T., 1994, Cosmic ray contributions to dose rates for luminescence and ESR dating: Large depths and long-term time variations: Radiation Measurements, v. 23, p. 497-500.

Sanderson, D.C.W., 1987, Thermoluminescence dating of vitrified Scottish Forts: Paisley, Paisley college.

Sanderson, D.C.W.1988, Thick source beta counting (TSBC): A rapid method for measuring beta dose-rates: International Journal of Radiation Applications and Instrumentation. Part D. Nuclear Tracks and Radiation Measurements, v. 14, p. 203-207.

Acknowledgements

Scottish Universities Environmental Research Centre

Appendix A: Dose response curves

A.1 Samples from 2015 fieldwork
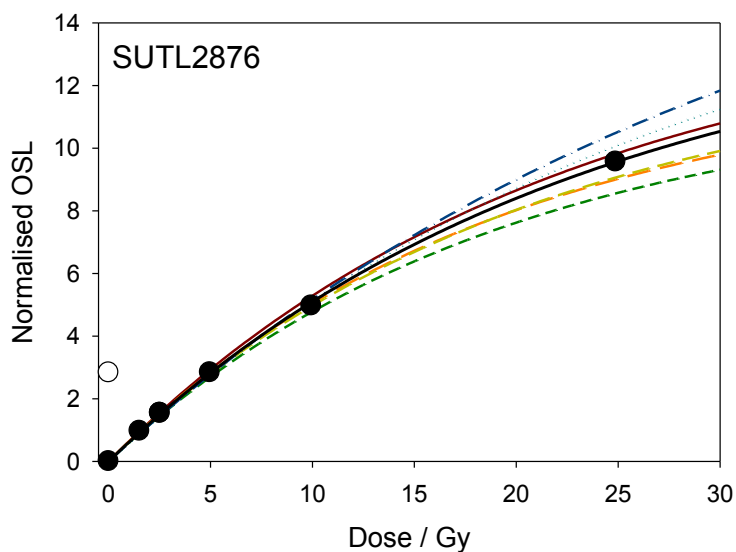
Figure A.1: Composite dose response curves for SUTL2876
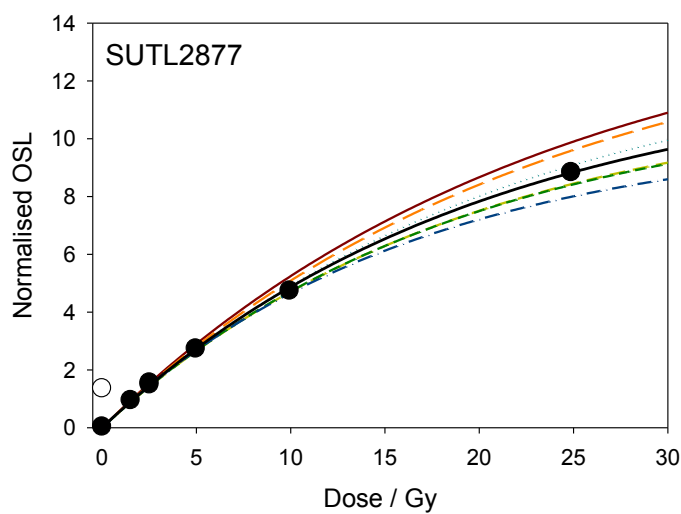
Figure A.2: Composite dose response curves for SUTL2877

Scottish Universities Environmental Research Centre
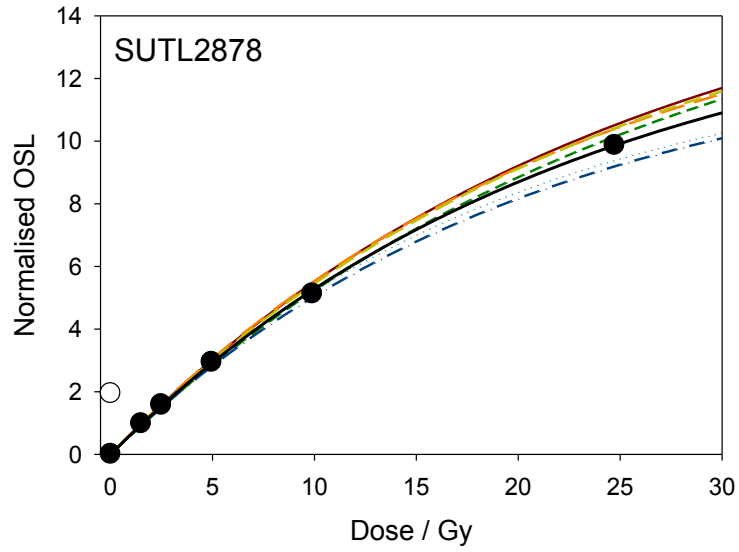
Figure A.3: Composite dose response curves for SUTL2878
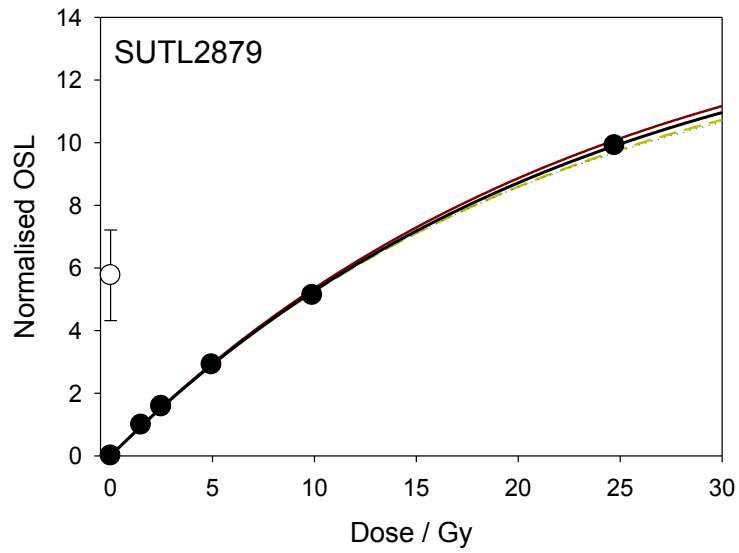
Figure A.4: Composite dose response curves for SUTL2879
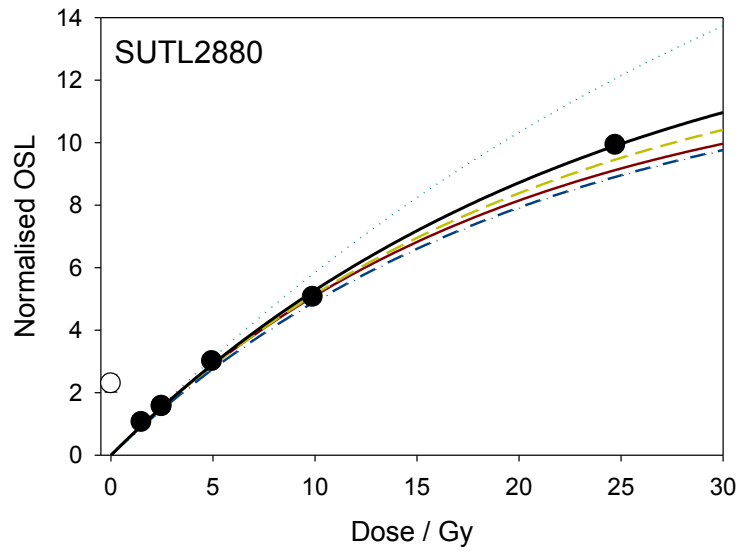
Figure A.5: Composite dose response curves for SUTL2880
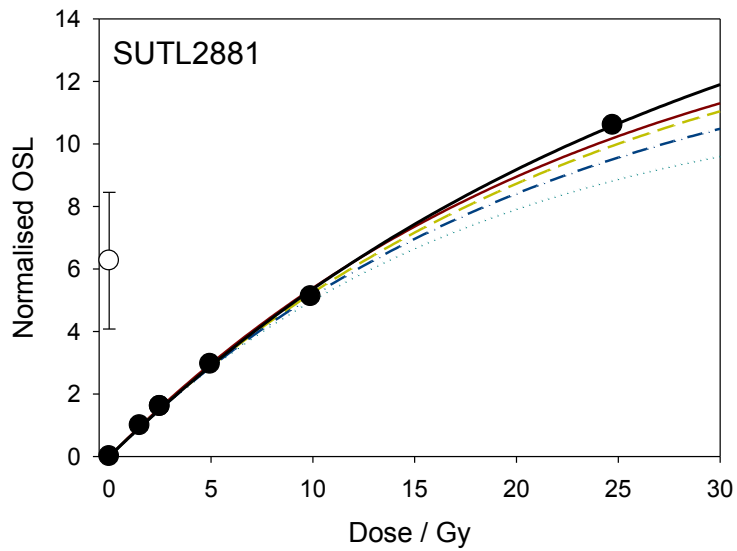
Figure A.6: Composite dose response curves for SUTL2881
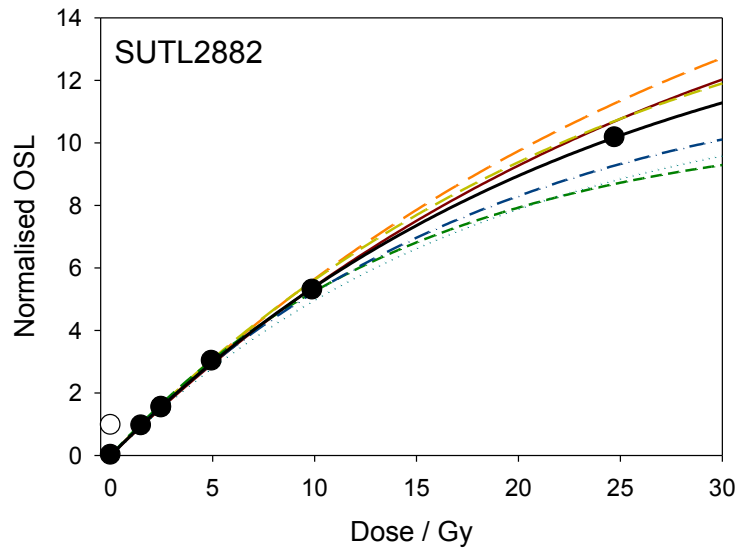
Figure A.7: Composite dose response curves for SUTL2882

A.2 Samples from 2016 fieldwork
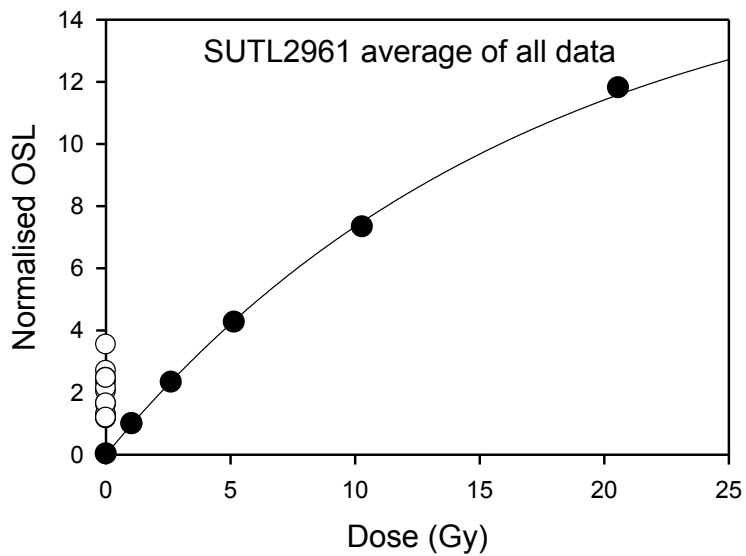
Figure A.8: Dose response curve for SUTL2961
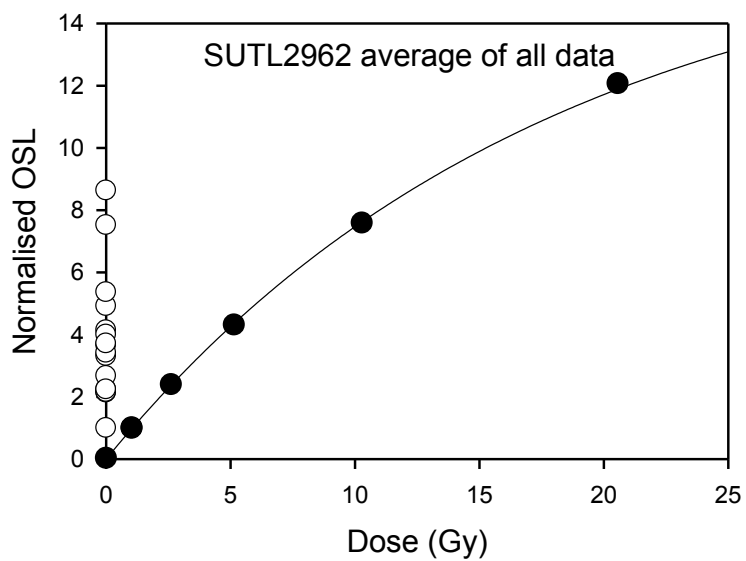
Figure A.9: Dose response curve for SUTL2962.
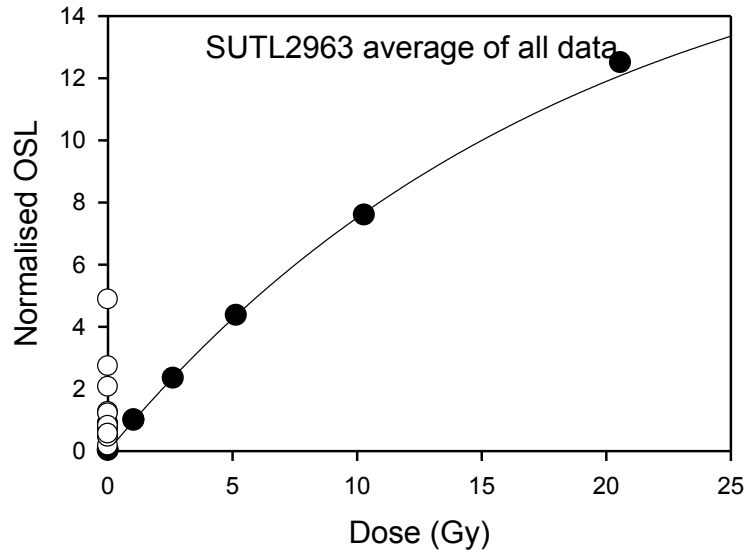
Figure A.10: Dose response curve for SUTL2963.
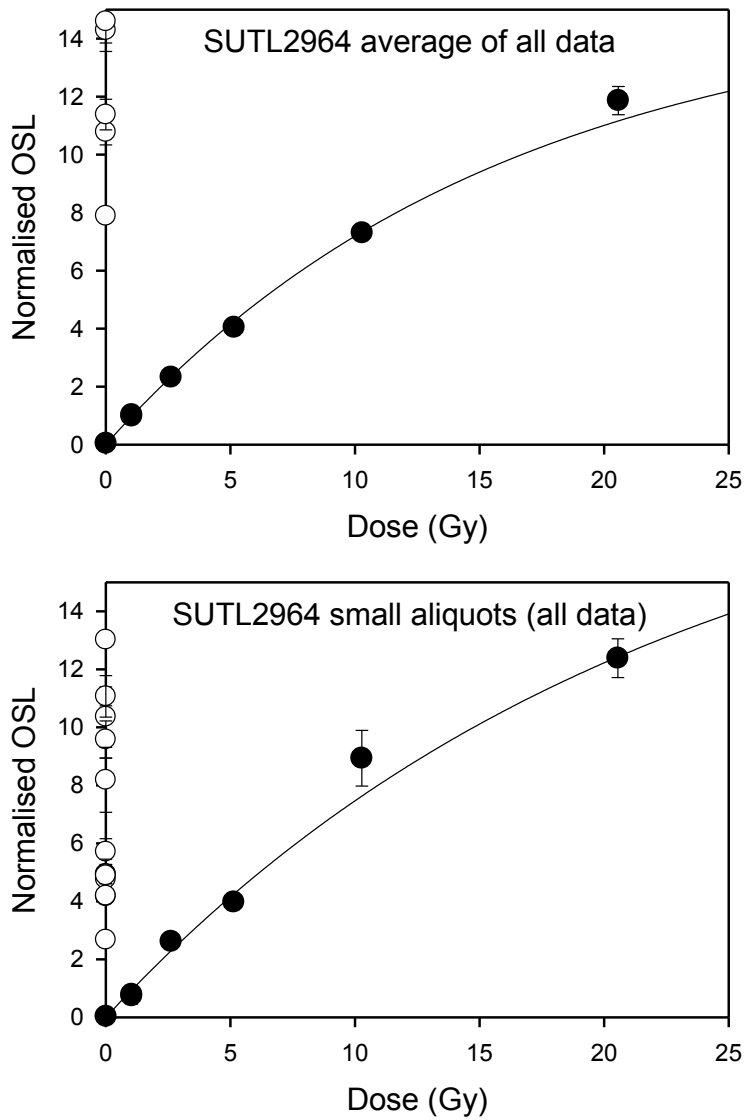
Figure A.11: Dose response curves for SUTL2964, for the initial large aliquots (top) and follow-up small aliquots (bottom).

Scottish Universities Environmental Research Centre
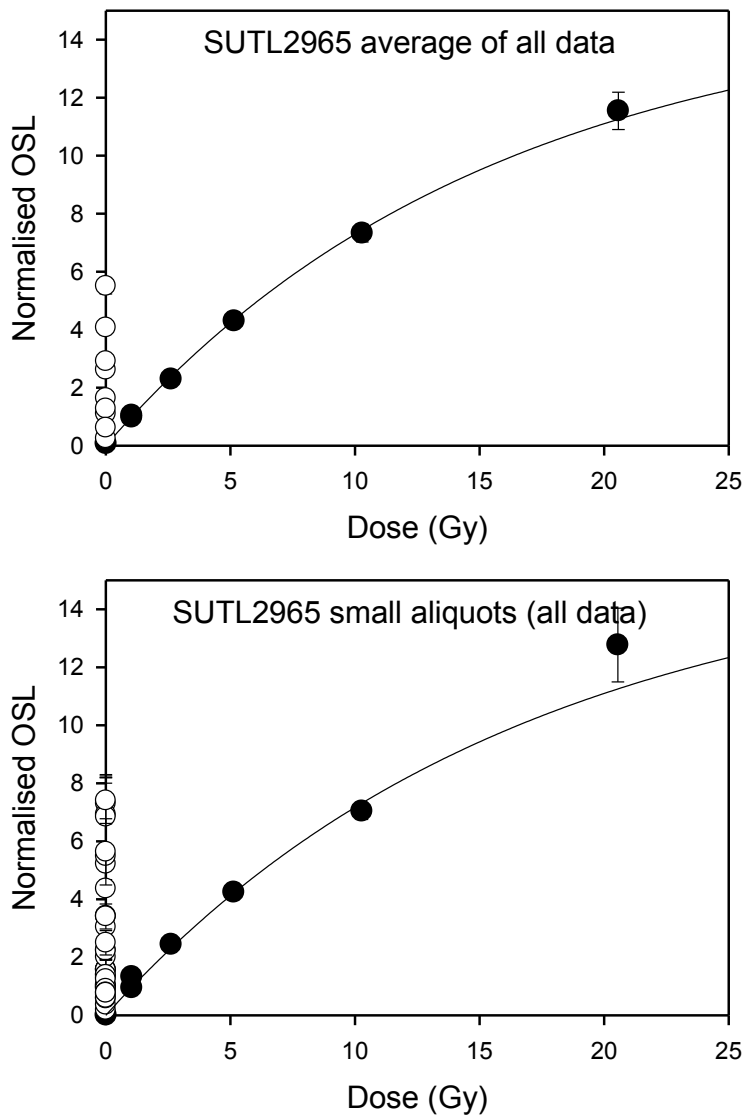
Figure A.12: Dose response curves for SUTL2965, for the initial large aliquots (top) and follow-up small aliquots (bottom).
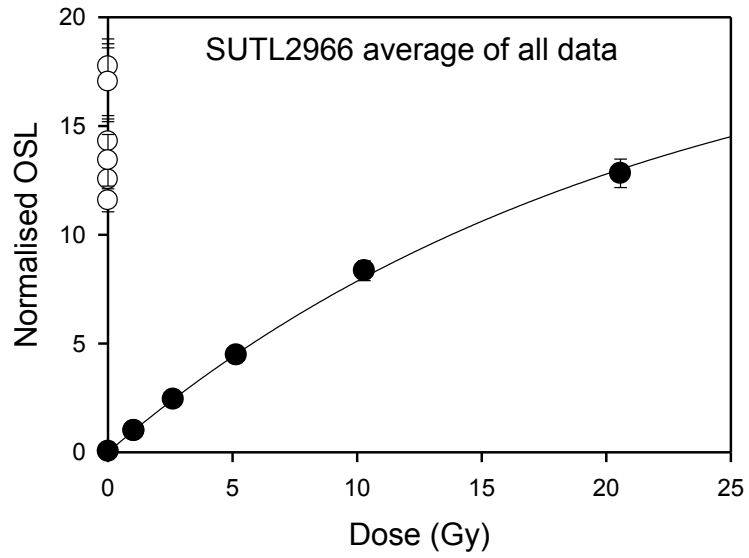
Figure A.13: Dose response curve for SUTL2966.
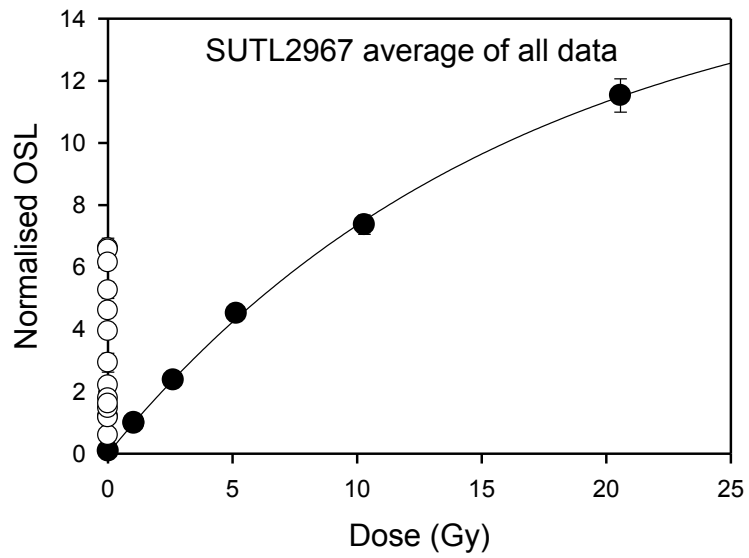
Figure A.14: Dose response curve for SUTL2967.

Appendix B: Kernel Density Estimate and Probability Density Function Plots

B.1. Samples from 2015 fieldwork
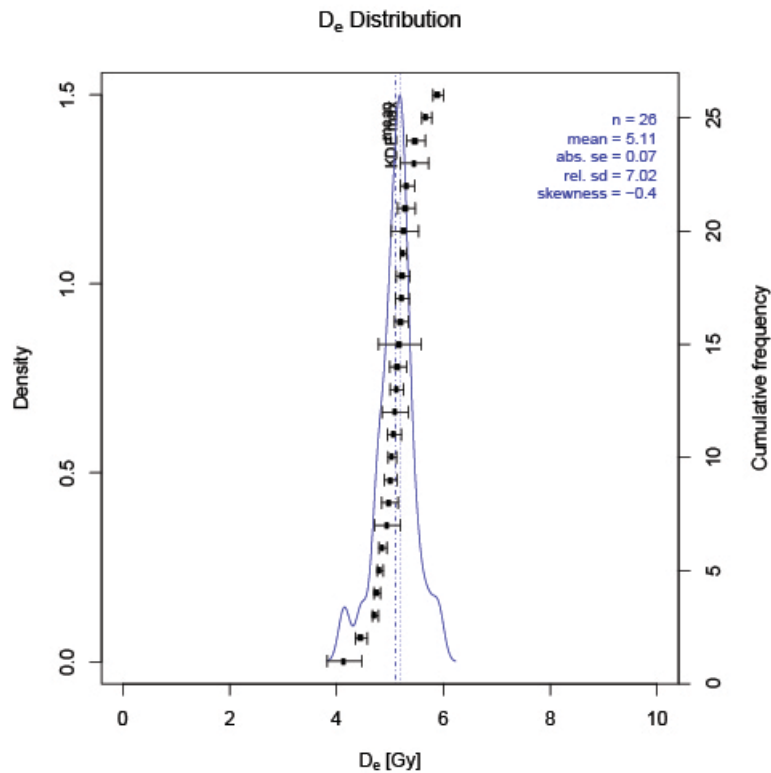
Figure B.1: KDE plot (after Dietze et al.) for SUTL2876
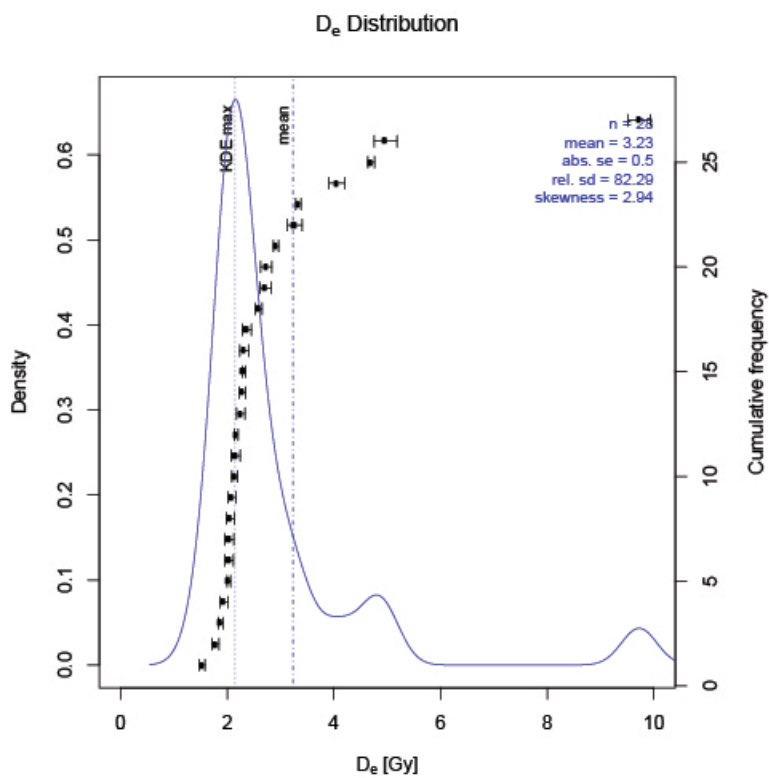
Figure B.2: KDE plot (after Dietze et al.) for SUTL2877
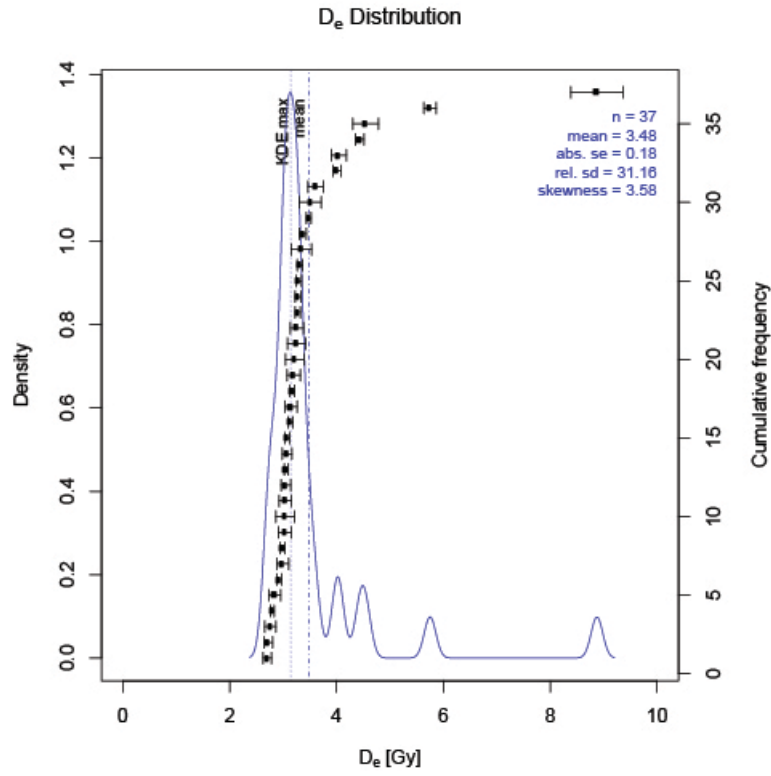
Figure B.3: KDE plot (after Dietze et al.) for SUTL2878
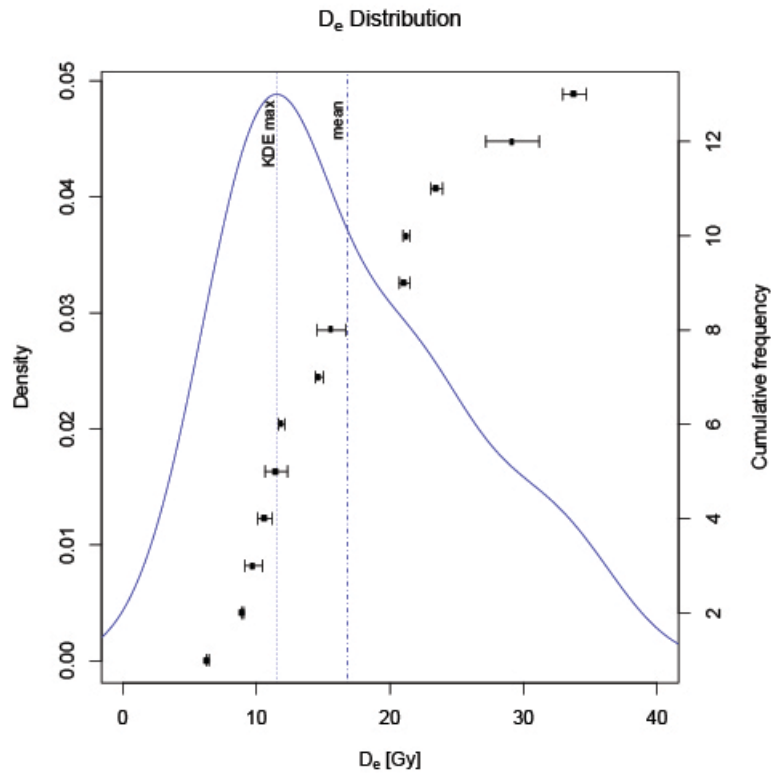
Figure B.4: KDE plot (after Dietze et al.) for SUTL2879
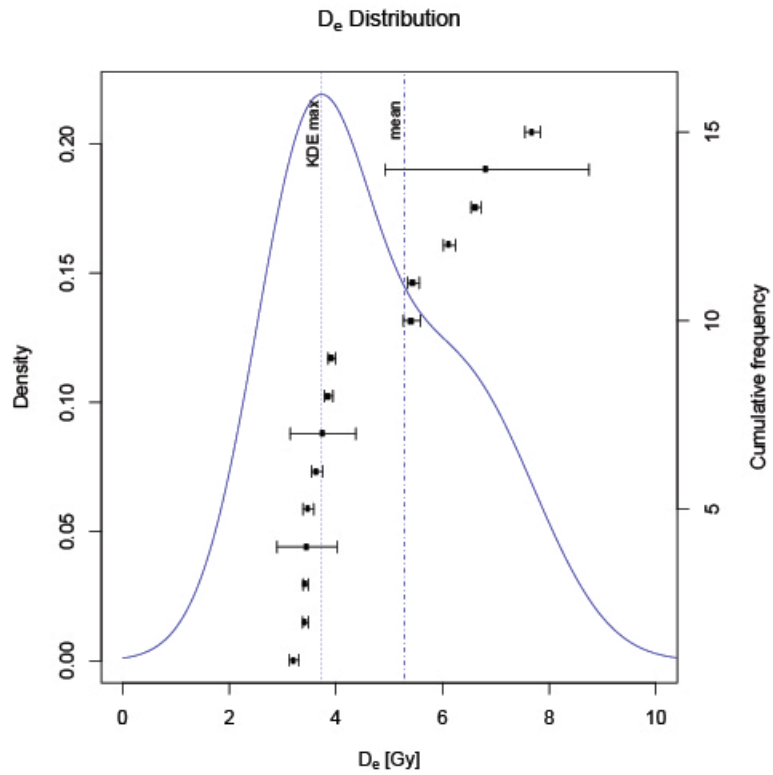
Figure B.5: KDE plot (after Dietze et al.) for SUTL2880
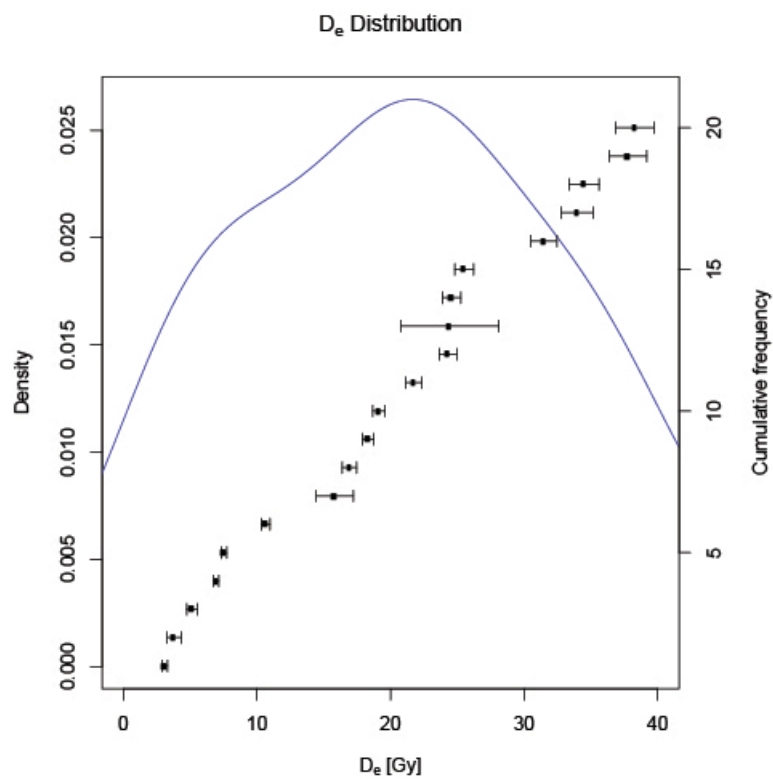
Figure B.6: KDE plot (after Dietze et al.) for SUTL2881
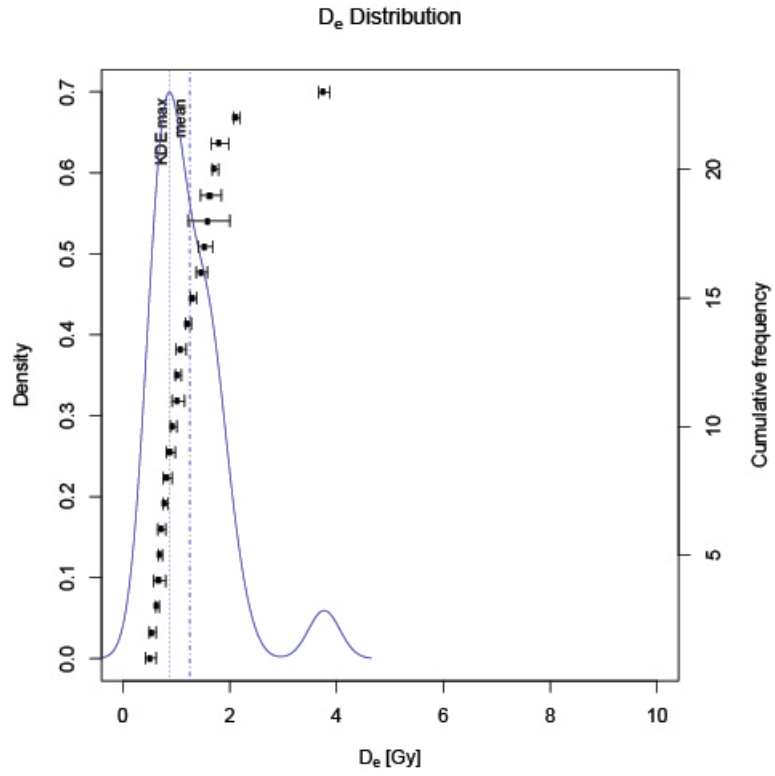
Figure B.7: KDE plot (after Dietze et al.) for SUTL2882

B.2 Samples from 2016 fieldwork

D_e Distribution
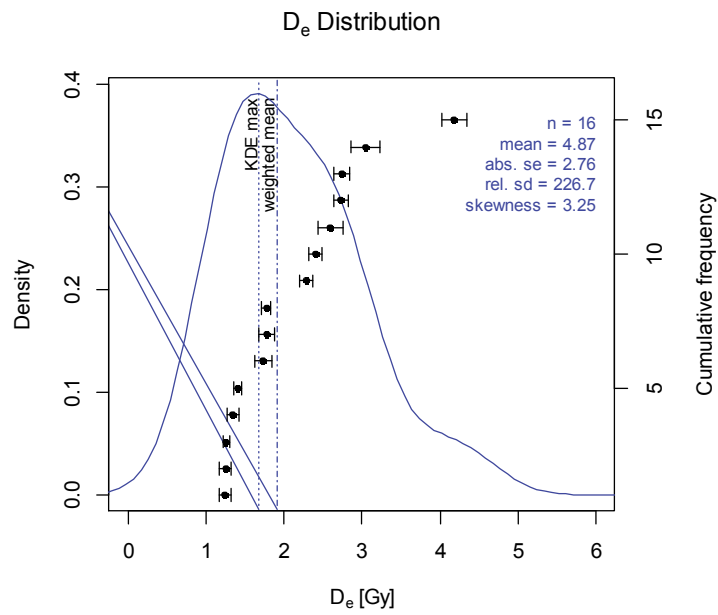
Figure B.8: KDE plot for SUTL2961; note it excludes aliquot at >45 Gy.
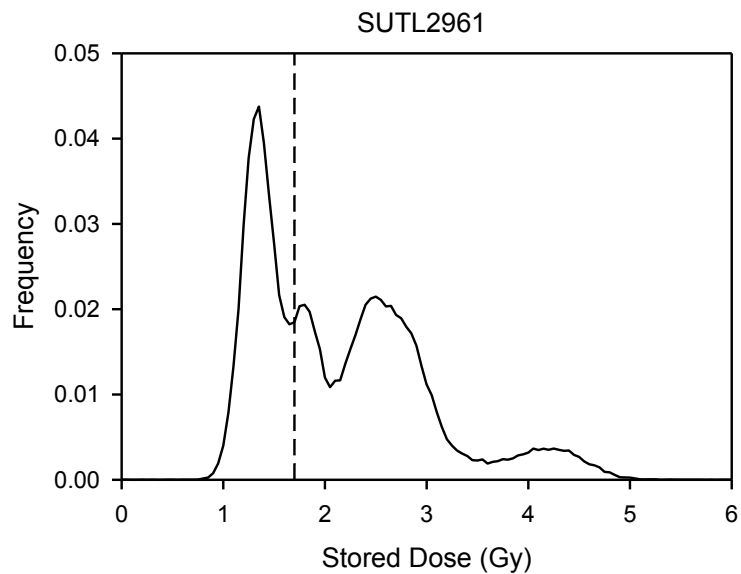
SUTL2961

Figure B.9: PDF plot for SUTL2961, with the weighted mean indicated; note aliquot >45 Gy excluded.
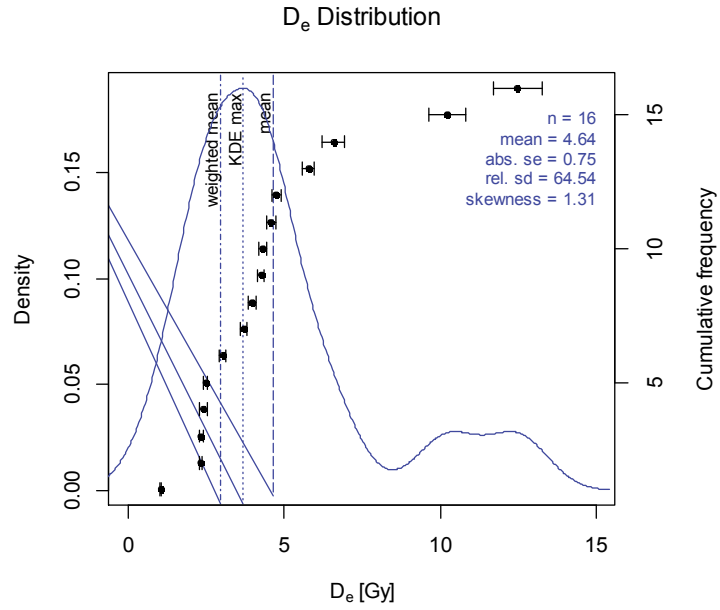
Figure B.10: KDE plot for SUTL2962
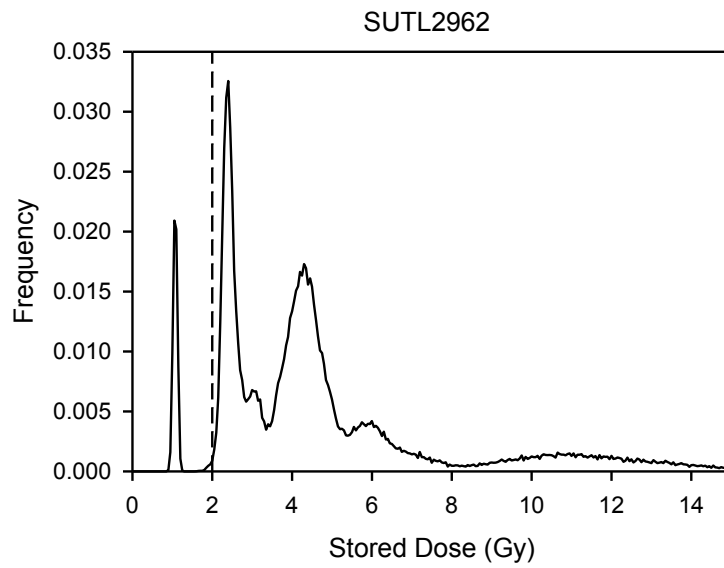
Figure B.11: PDF plot for SUTL2962, indicating the weighted mean.
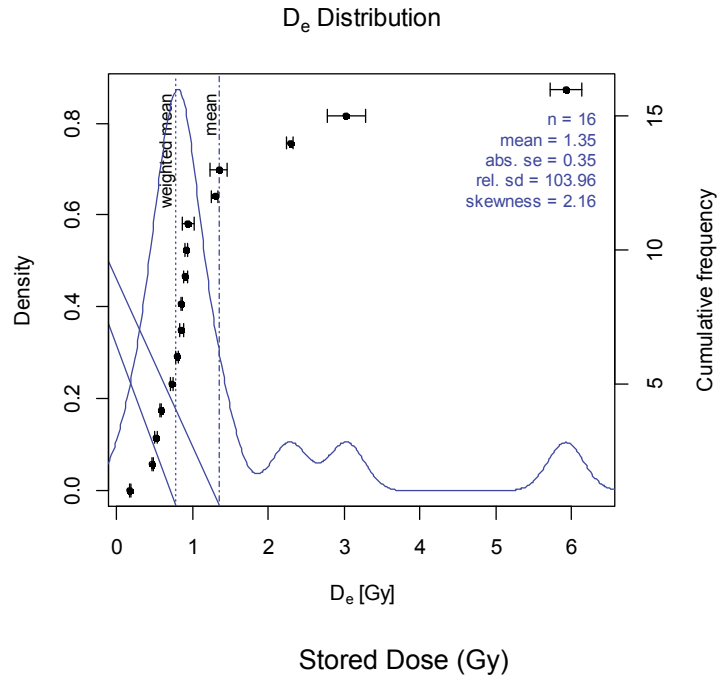
Figure B.12: KDE plot for SUTL2963.
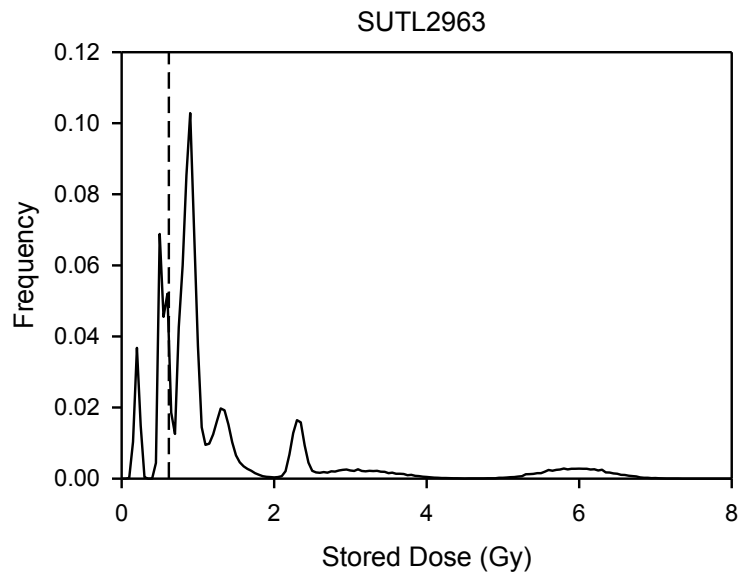
Figure B.13: PDF plot for SUTL2963, with the weighted mean indicated.
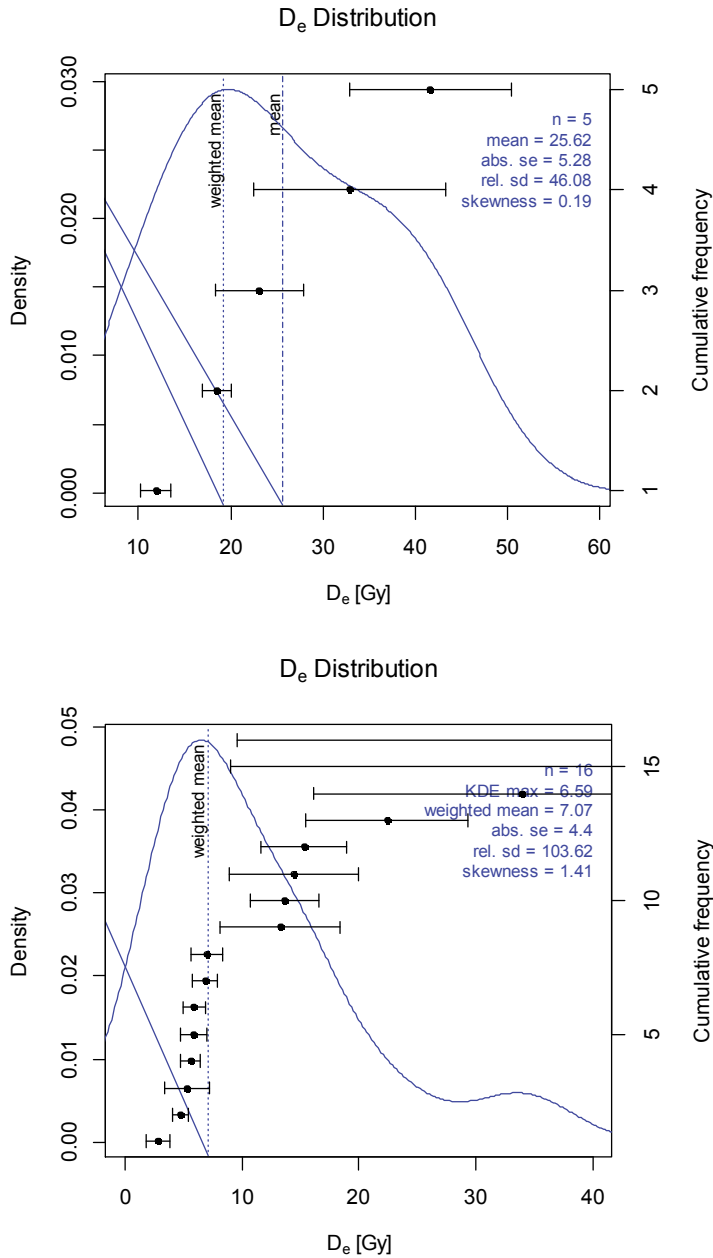
Figure B.14: KDE plots for SUTL2964; top for 16 large aliquots (five non-saturated aliquots that satisfy quality controls, excluding seven saturated aliquots), bottom for 48 small aliquots (excluding eleven saturated aliquots).
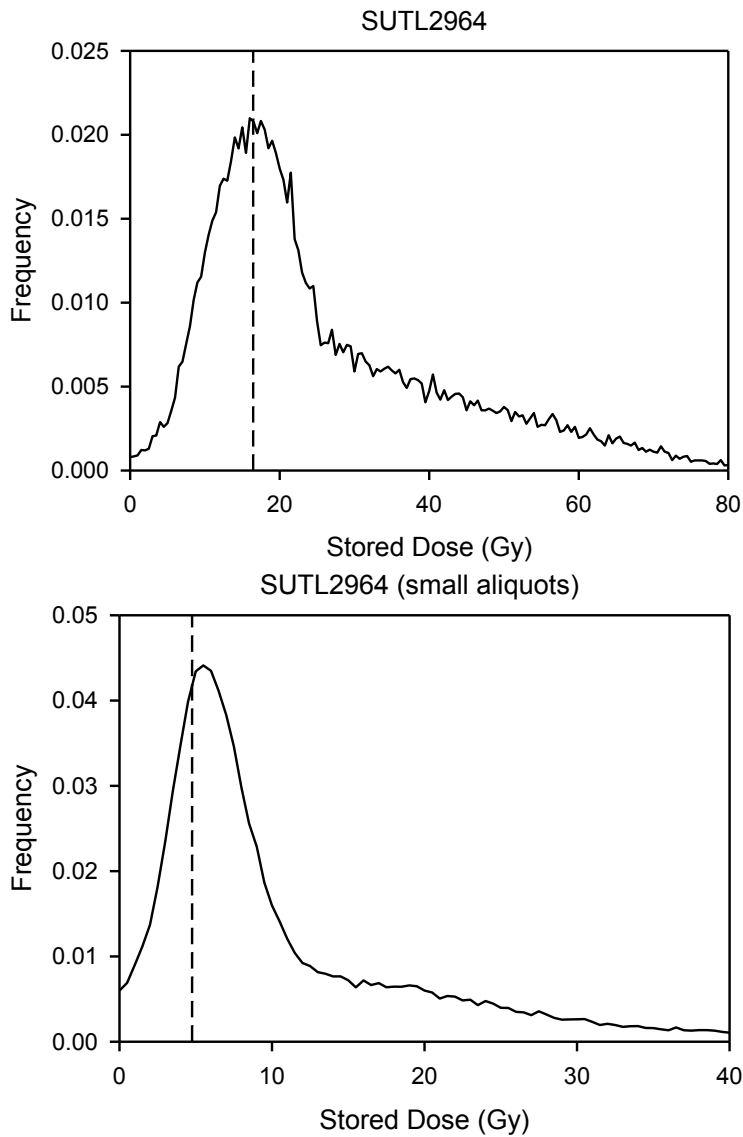
Figure B.15: PDF plots for SUTL2964; top for 16 large aliquots (excluding seven saturated aliquots), bottom for 48 small aliquots (excluding eleven saturated aliquots). With the weighted means indicated.
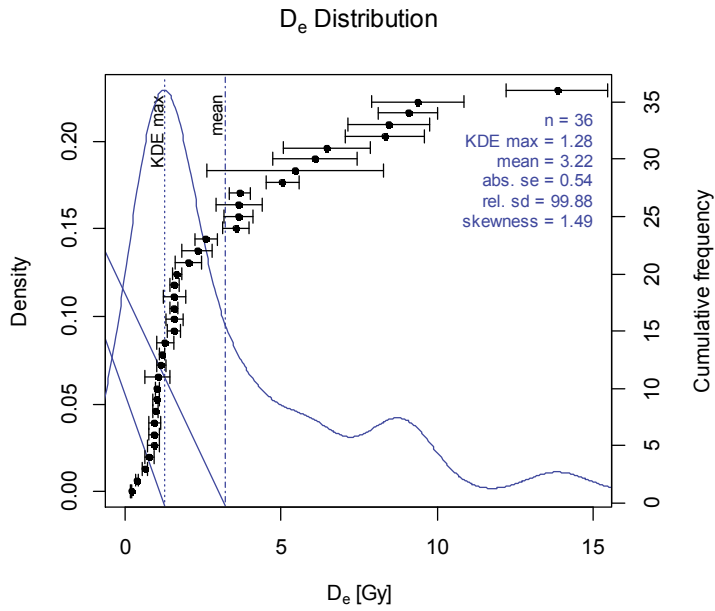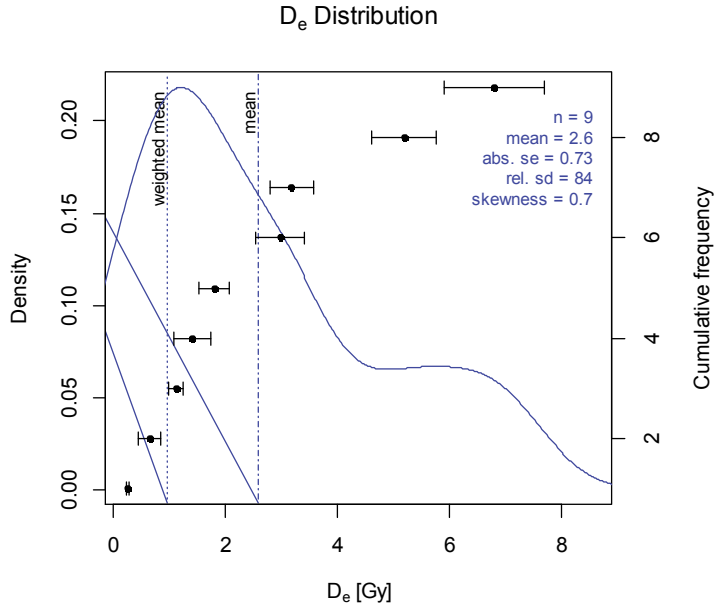
Figure B.16: KDE plots for SUTL2965; top for large aliquots (excluding one saturated aliquot), bottom for small aliquots (excluding one saturated aliquot).
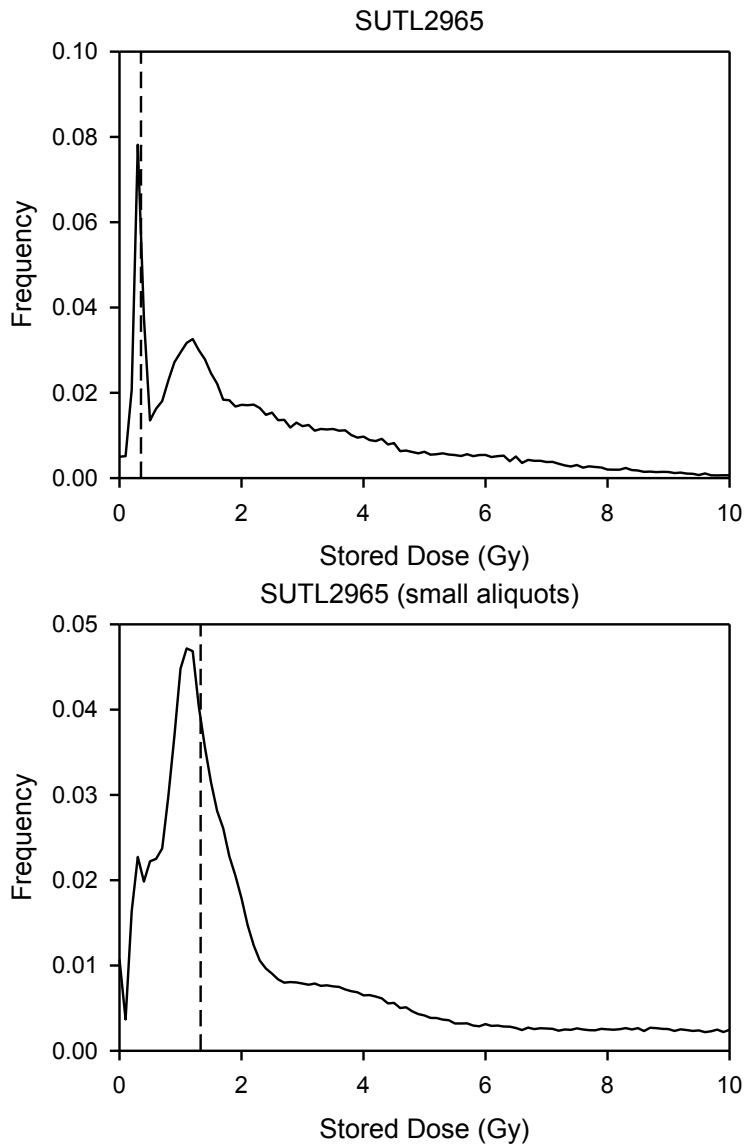
Figure B.17: PDF plots for SUTL2965; top for large aliquots (excluding one saturated aliquot), bottom for small aliquots (excluding one saturated aliquot). With the weighted means indicated.
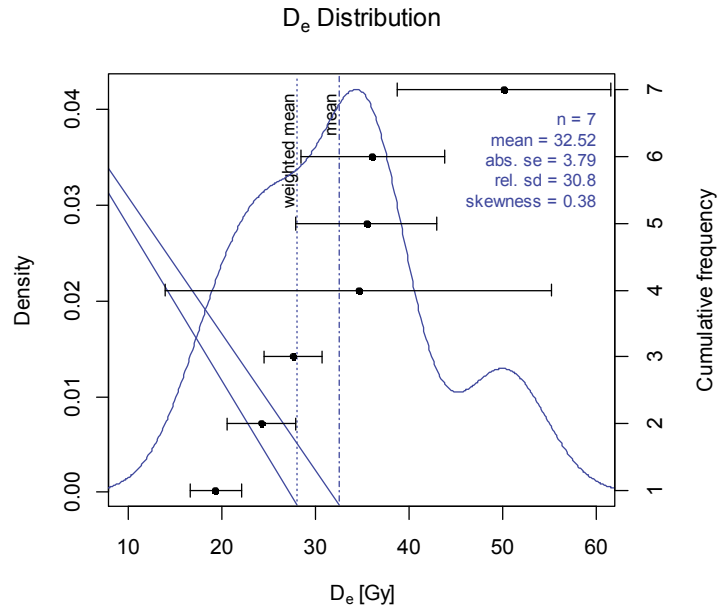
Figure B.18: KDE plot for SUTL2966 for seven non-saturating aliquots that satisfy quality criteria, excluding three saturated discs.
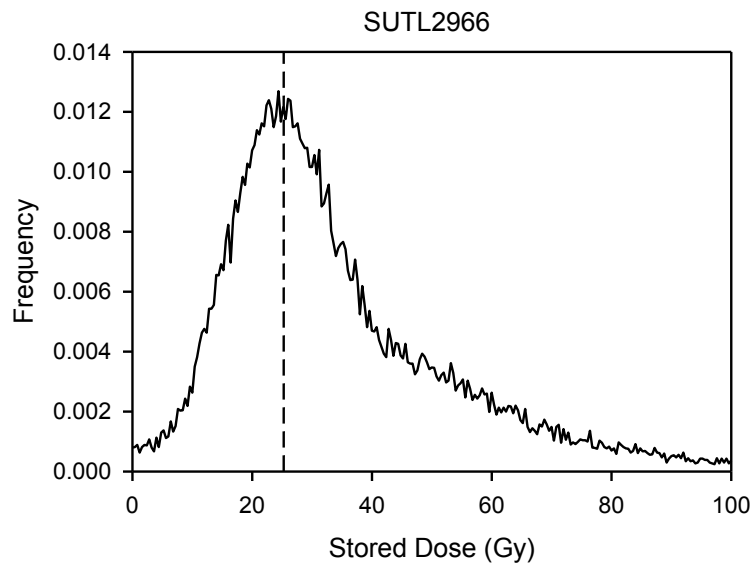
Figure B.19: PDF plot for SUTL2966 for seven non-saturating aliquots that satisfy quality criteria, excluding three saturated discs, with the weighted mean indicated.

D_e Distribution

n = 14
mean = 4.1
abs. se = 0.81
rel. sd = 74.02
skewness = 0.47
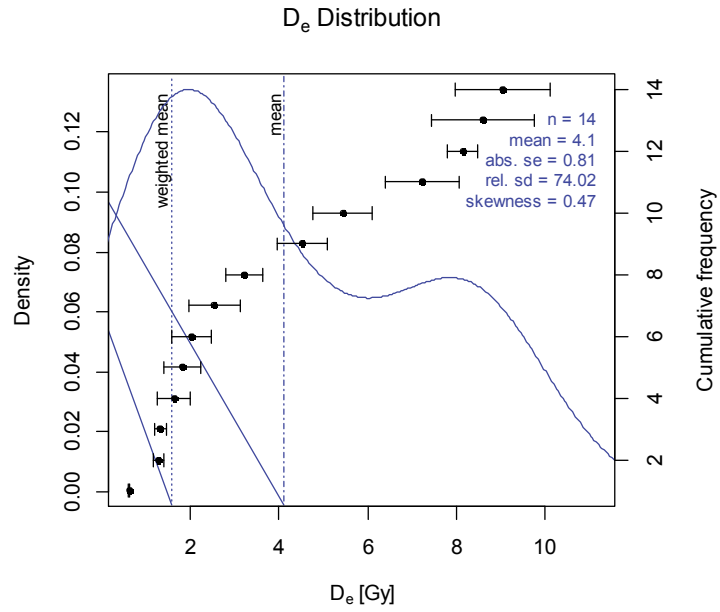
Figure B.20: KDE plot for SUTL2967.
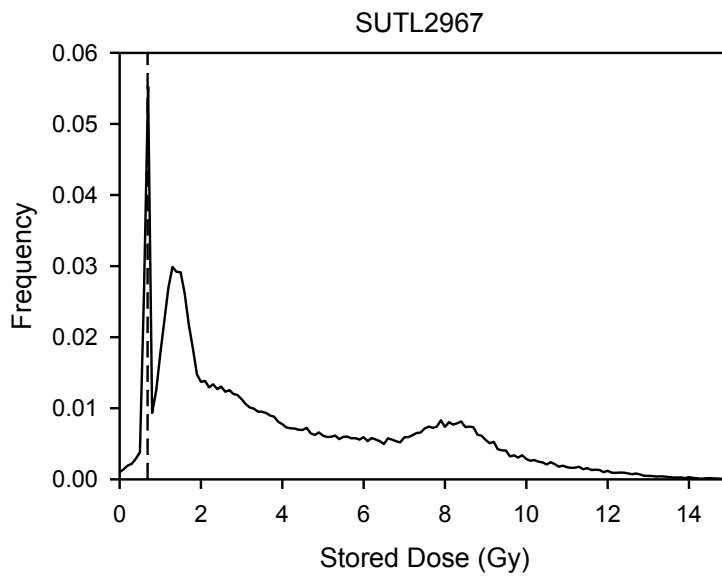
SUTL2967

Figure B.21: PDF plot for SUTL2967.

Appendix C: Abanico Plots

C.1: Samples from 2015 fieldwork
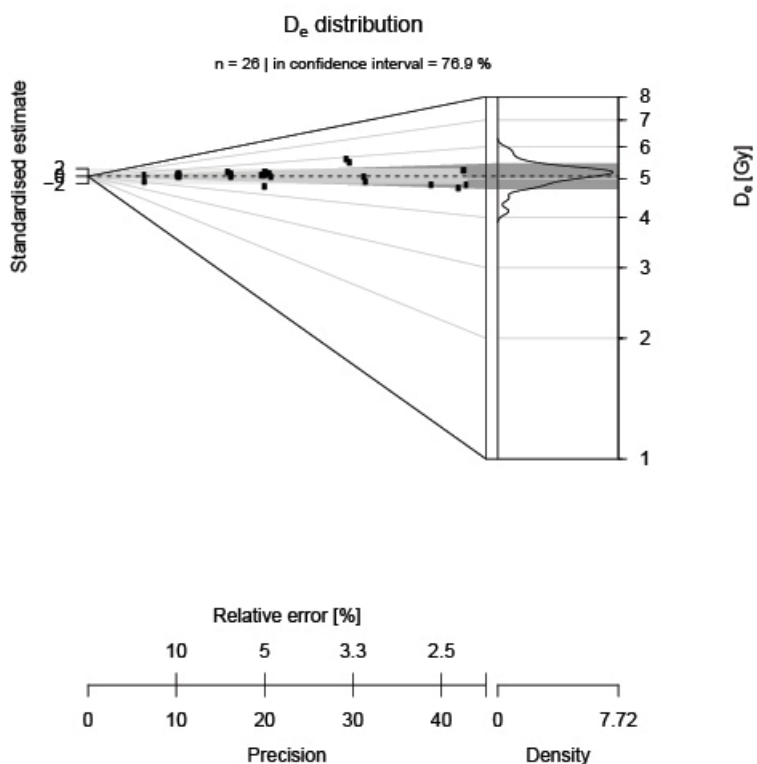
Figure C.1: Abanico plot (after Dietze et al.) for SUTL2876
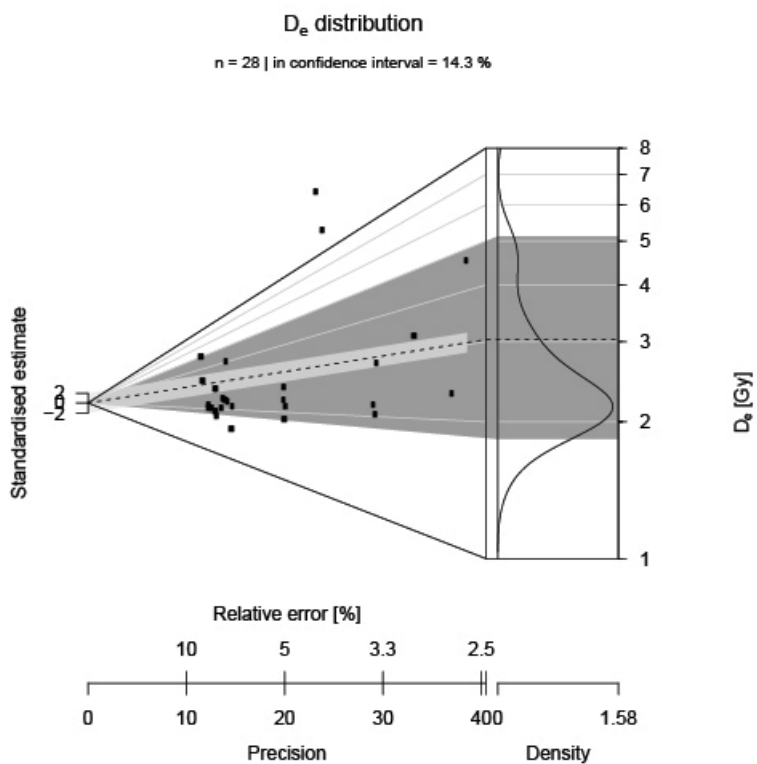
Figure C.2: Abanico plot for SUTL2877
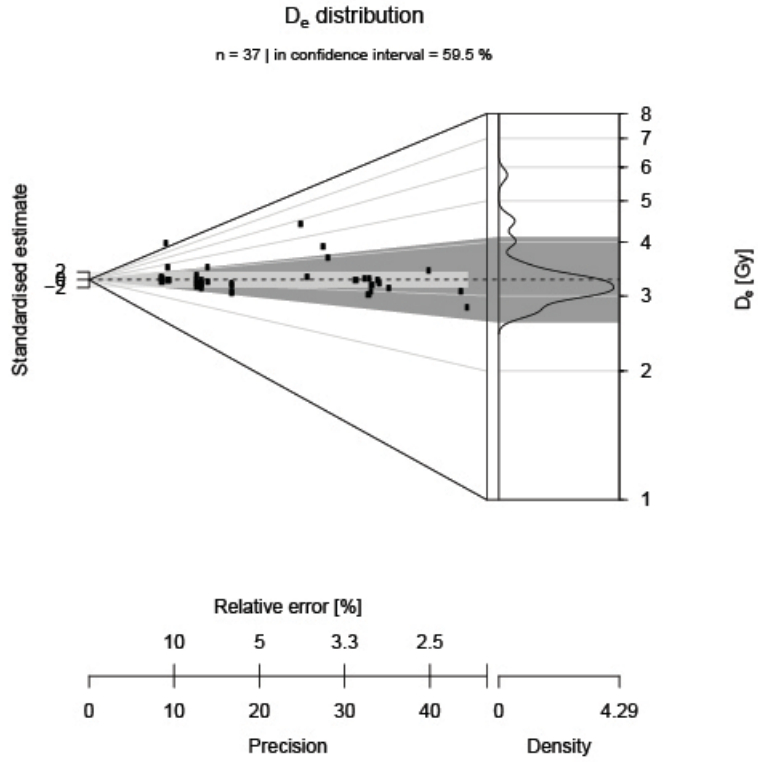
Figure C.3: Abanico plot for SUTL2878
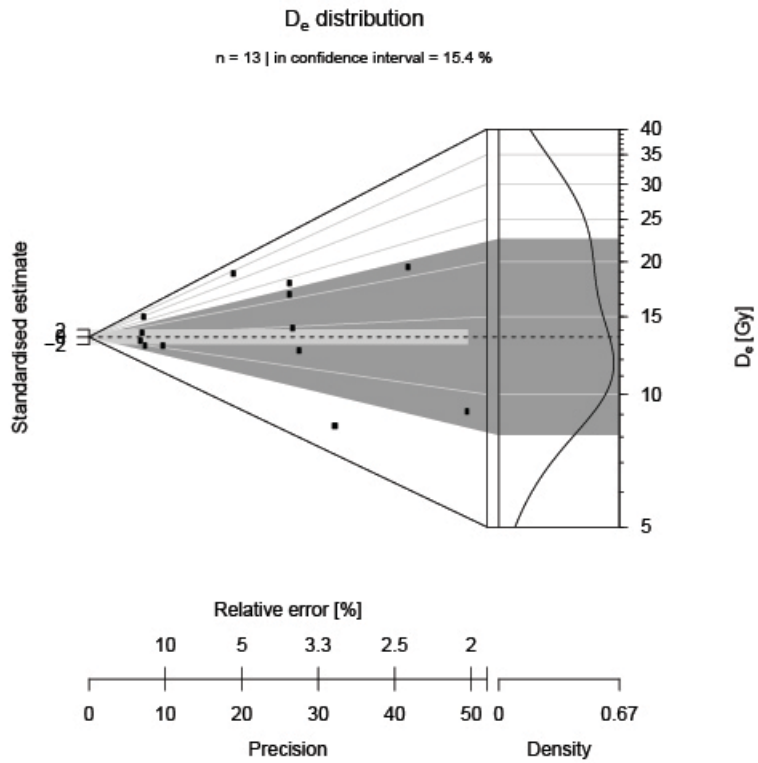
Figure C.4: Abanico plot for SUTL2879
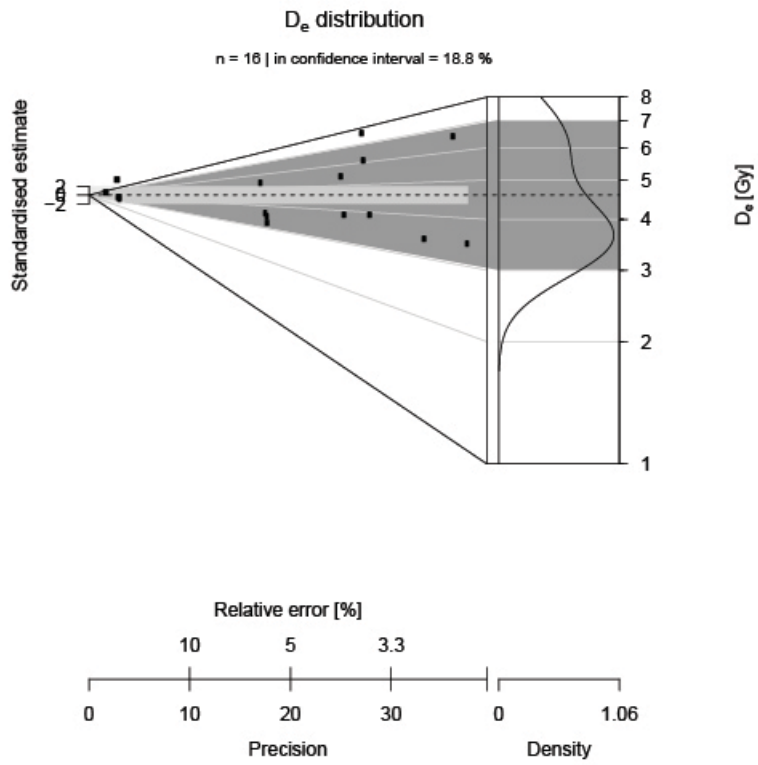
Figure C.5: Abanico plot for SUTL2880
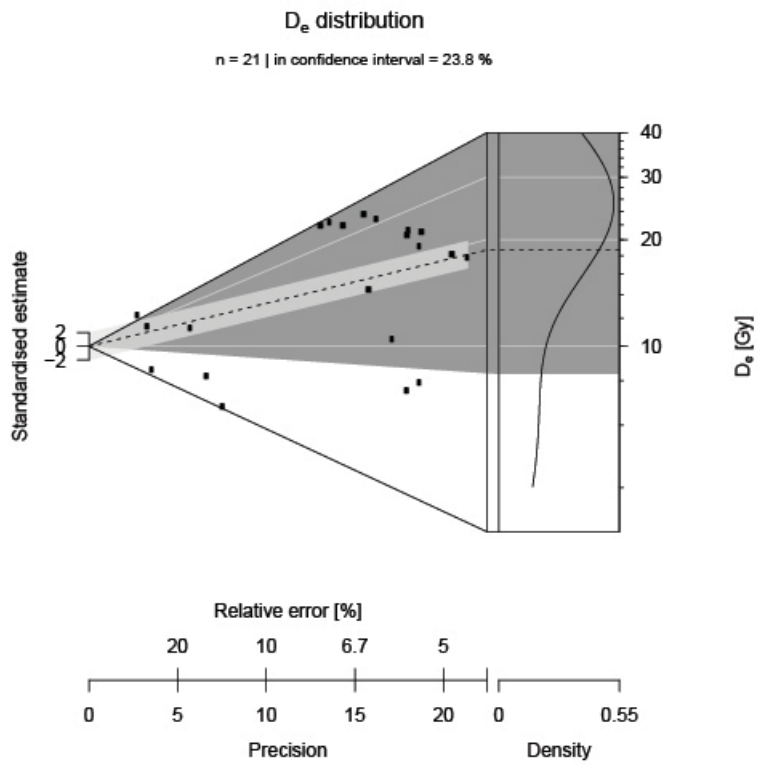
Figure C.6: Abanico plot for SUTL2881
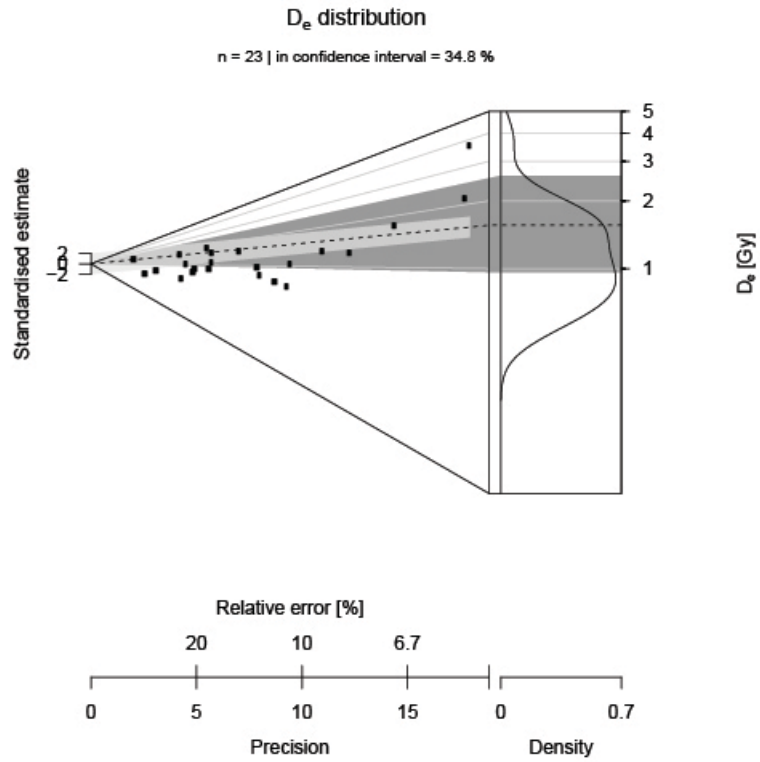
Figure C.7: Abanico plot for SUTL2882

C.2 Samples from 2016 fieldwork
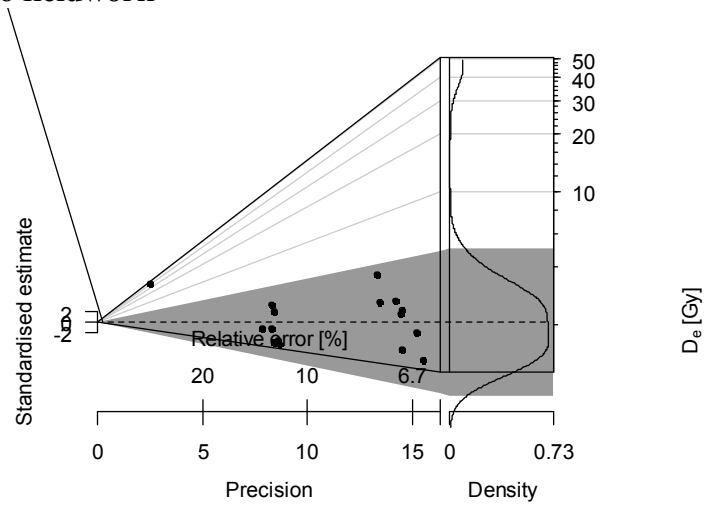
Figure C.8: Abanico plot for SUTL2961. The dashed line indicates the robust mean value (2.15 Gy)
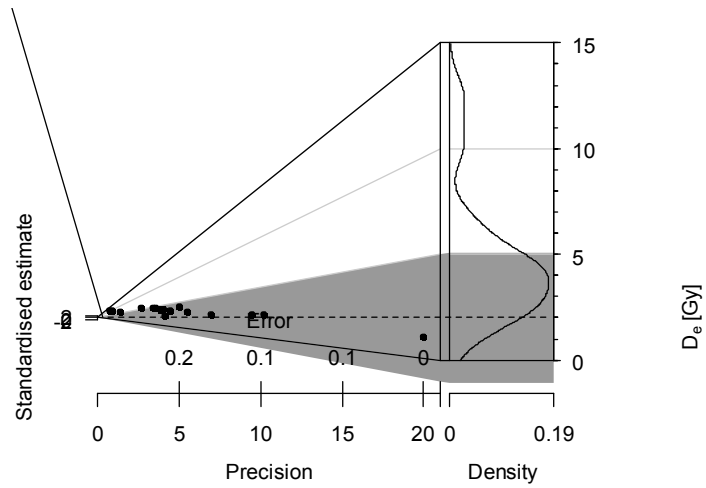
Figure C.9: Abanico plot for SUTL2962, the dashed line indicates the weighted mean.
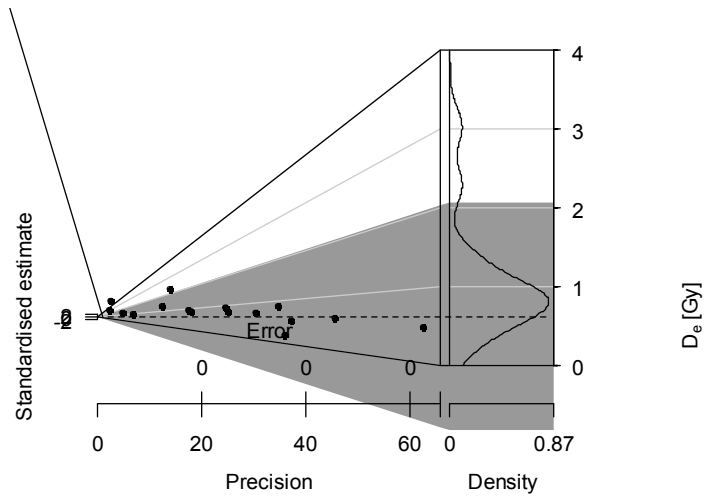
Figure C.10: Abanico plot for SUTL2963, the dashed line indicates the weighted mean.
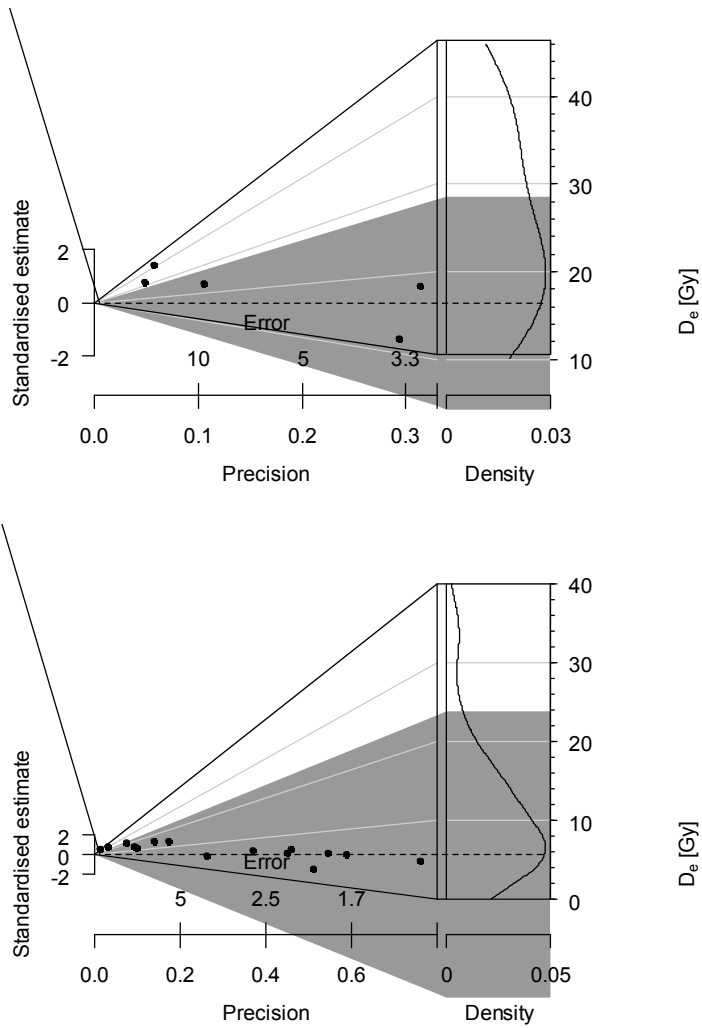
Figure C.11: Abanico plots for SUTL2964; top for large aliquots (five non-saturated aliquots that satisfy quality controls, excluding seven saturated aliquots), bottom for small aliquots (excluding eleven saturated aliquots). With the weighted means indicated.
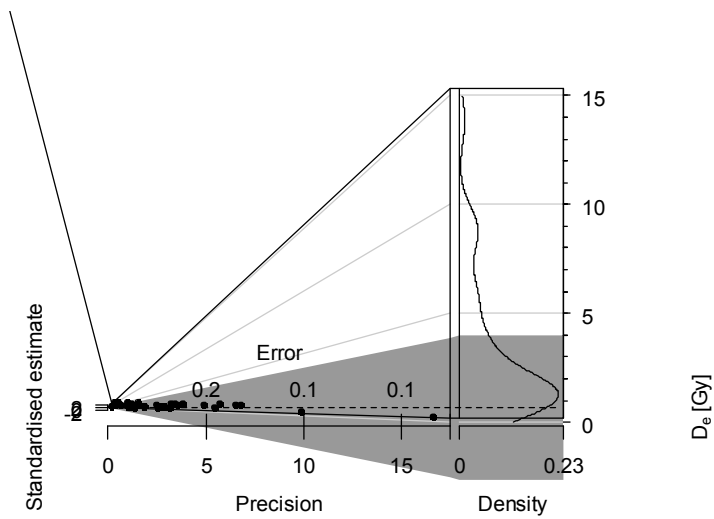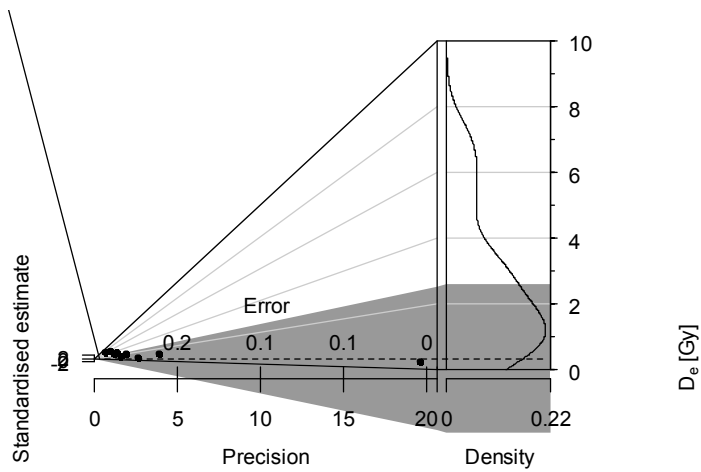
Figure C.12: Abanico plots for SUTL2965; top for large aliquots (excluding one saturated aliquot), bottom for small aliquots (excluding one saturated aliquot). With the weighted means indicated.
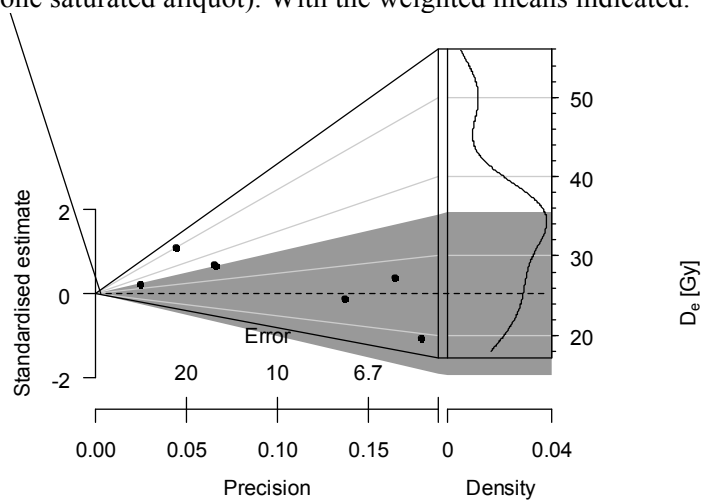

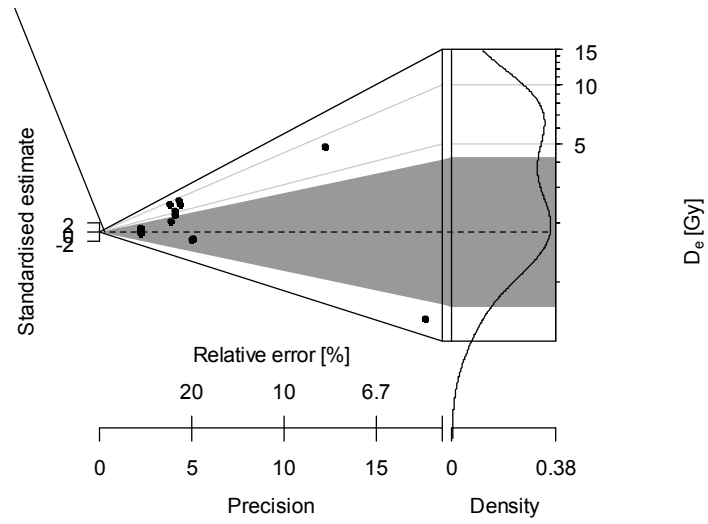Figure C.13: Abanico plot for SUTL2966 for seven non-saturating aliquots that satisfy quality criteria, excluding three saturated discs.

Figure C.14: Abanico plot for SUTL2967.